



# Rates and Properties of Supernovae Strongly Gravitationally Lensed by Elliptical Galaxies in Time-domain Imaging Surveys

Daniel A. Goldstein<sup>1,2,3,5</sup> , Peter E. Nugent<sup>2,3</sup> , and Ariel Goobar<sup>4</sup>

<sup>1</sup> California Institute of Technology, 1200 East California Blvd, MC 249-17, Pasadena, CA 91125, USA

<sup>2</sup> Lawrence Berkeley National Laboratory, 1 Cyclotron Road MS 50B-4206, Berkeley, CA, 94720, USA

<sup>3</sup> Department of Astronomy, University of California, Berkeley, 501 Campbell Hall, Berkeley, CA 94720, USA

<sup>4</sup> The Oskar Klein Centre, Department of Physics, Stockholm University, AlbaNova, SE-106 91 Stockholm, Sweden

Received 2018 September 26; revised 2019 April 30; accepted 2019 May 6; published 2019 July 1

## Abstract

Supernovae that are strongly gravitationally lensed (gLSNe) by elliptical galaxies are powerful probes of astrophysics and cosmology that will be discovered systematically by wide-field, high-cadence imaging surveys such as the Zwicky Transient Facility (ZTF) and the Large Synoptic Survey Telescope (LSST). Here we use pixel-level simulations that include observing strategy, target selection, supernova properties, and dust to forecast the rates and properties of gLSNe that ZTF and LSST will find. Applying the resolution-insensitive discovery strategy of Goldstein et al., we forecast that ZTF (LSST) can discover 0.02 (0.79) 91bg-like, 0.17 (5.92) 91T-like, 1.22 (47.84) Type Ia, 2.76 (88.51) Type IIP, 0.31 (12.78) Type IIL, and 0.36 (15.43) Type Ib/c gLSNe per year, with uncertainties dominated by uncertainties in the supernova rate. We also forecast that the surveys can discover at least 3.75 (209.32) Type IIn gLSNe per year, for a total of at least 8.60 (380.60) gLSNe per year under fiducial observing strategies. ZTF gLSNe have a median  $z_s = 0.9$ ,  $z_l = 0.35$ ,  $|\mu_{\text{tot}}| = 30$ ,  $\Delta t_{\text{max}} = 10$  days,  $\min(\theta) = 0.^{\circ}25$ , and  $N_{\text{img}} = 4$ . LSST gLSNe are less compact and less magnified, with a median  $z_s = 1.0$ ,  $z_l = 0.4$ ,  $|\mu_{\text{tot}}| = 6$ ,  $\Delta t_{\text{max}} = 25$  days,  $\min(\theta) = 0.^{\circ}6$ , and  $N_{\text{img}} = 2$ . We develop a model of the supernova–host galaxy connection and find that the vast majority of gLSN host galaxies will be multiply imaged, enabling detailed constraints on lens models with sufficiently deep high-resolution imaging taken after the supernova has faded. We release the results of our simulations as catalogs at <http://portal.nersc.gov/project/astro250/glsne/>.

**Key words:** gravitational lensing: strong – supernovae: general

## 1. Introduction

When a supernova explodes far behind a foreground galaxy, the galaxy’s strong gravitational field can create multiple images of the supernova in different places on the sky (Einstein 1936; Zwicky 1937). Because these images travel along different geometric paths and through different gravitational potentials to reach us, they arrive at different times, and in general they can be highly magnified (Refsdal 1964a). Time delays between the multiple images of these “strongly gravitationally lensed supernovae” (gLSNe) can be used to measure the Hubble constant  $H_0$  (Refsdal 1964b), which is currently in tension at the  $4.4\sigma$  level (Riess et al. 2019), independent of the local distance ladder and the assumed cosmological model (e.g., Birrer et al. 2019). If a gLSN is discovered before all of its images arrive, early moments of the supernova can be observed by anticipating the appearance of the remaining images (e.g., Goldstein et al. 2018; Suwa 2018). These remarkable attributes make gLSNe valuable probes of astrophysics and cosmology.

To date, only two gLSNe with resolved images have been discovered (Kelly et al. 2015; Goobar et al. 2017). Neither has yielded competitive constraints on  $H_0$  (but see Bonvin et al. 2017; Suyu et al. 2017; Grillo et al. 2018; Vega-Ferrero et al. 2018), nor observations of the earliest moments of the supernova light curve. However, a new generation of high-cadence, wide-field imaging surveys, exemplified by the Zwicky Transient Facility (ZTF; 2018–2021; Graham et al. 2019), the Large Synoptic Survey Telescope (LSST;

2021–2033; LSST Science Collaboration et al. 2009), and the *Wide-Field Infrared Survey Telescope* (WFIRST; 2025–2031; Spergel et al. 2013), is expected to yield thousands of gLSNe over the next decade (Goldstein & Nugent 2017; Goldstein et al. 2018, see also Oguri & Marshall 2010). These surveys will cover enough of the sky, to sufficient depth and at high-enough cadence, to produce the first statistical samples of gLSNe. They will also be the first to employ novel detection techniques that will eliminate the need to resolve multiple images for gLSN discovery, furthering the yield. Finally, they will implement highly tuned gLSN filters that will lead to early discovery and minimization of false positives.

To calibrate scientific expectations for the gLSN era, reliable forecasts of gLSN yields and properties are needed. Schneider & Wagoner (1987) and Linder et al. (1988) carried out the first gLSN property forecasts, and Kolatt & Bartelmann (1998), Sullivan et al. (2000), Holz (2001), Dobler & Keeton (2006), Oguri & Marshall (2010), Goldstein & Nugent (2017), Goldstein et al. (2018), and Shu et al. (2018) presented refined calculations. Each of these studies neglected to account for at least one of the following important effects: observing strategy and conditions, dust, discovery strategy, multiple supernova subtypes and rates, and the supernova–host galaxy connection. In anticipation of the gLSN era, we present the first pixel-level Monte Carlo, ray-tracing, and image simulations of the gLSN population to include a detailed treatment of these important effects and use them to forecast gLSN rates and properties. In Section 2, we describe our models of the supernova, host galaxy, deflector, and lens galaxy populations. In Section 3, we present the results of our simulations, including gLSN yields and time delay, brightness, and image

<sup>5</sup> Hubble Fellow.

separation distributions. We discuss the implications of our results in Section 4 and conclude in Section 5. In our calculations, we assume a Planck Collaboration et al. (2016) cosmology.

## 2. Population Models

In this section, we describe the models of the deflector, lens galaxy, supernova, and host galaxy populations that we use to forecast the rates and properties of gLSNe from upcoming surveys.

### 2.1. Deflectors

Although galaxy clusters and late-type galaxies can act as gravitational lenses for background supernovae, we consider only elliptical galaxies as lenses in this analysis. In addition to being the most common type of gravitational lens, dominating the lensing cross section over clusters and late-type galaxies, ellipticals are the only lens galaxies that are compatible with the discovery strategy we use in our forecasts (see Section 2.9), and their mass profiles are simpler to model than those of galaxy clusters, making them ideal for cosmological analyses. The gLSN yields presented in this article are therefore lower limits on the true achievable gLSN yields of future surveys.

We model the projected mass distribution of elliptical galaxies as a singular isothermal ellipsoid (SIE; Kormann et al. 1994), which has shown excellent agreement with observations (e.g., Koopmans et al. 2009). The SIE convergence  $\kappa$  is given by

$$\kappa(x, y) = \frac{\theta_E}{2} \frac{\lambda(e)}{\sqrt{(1 - e)^{-1}x^2 + (1 - e)y^2}}, \quad (1)$$

where

$$\theta_E = 4\pi \left(\frac{\sigma}{c}\right)^2 \frac{D_{ls}}{D_s}. \quad (2)$$

In the above equations,  $\sigma$  is the velocity dispersion of the lens galaxy,  $e$  is its ellipticity, and  $\lambda(e)$  is its so-called “dynamical normalization,” a parameter related to three-dimensional shape, and  $D_{ls}$  and  $D_s$  are the angular diameter distances between the lens and the source and the observer and the source, respectively. Here we make the simplifying assumption that there are an equal number of oblate and prolate galaxies, which Chae (2003) showed implies  $\lambda(e) \simeq 1$ . We model the velocity distribution of elliptical galaxies as a modified Schechter function (Sheth et al. 2003):

$$dn = \phi(\sigma)d\sigma = \phi_* \left(\frac{\sigma}{\sigma_*}\right)^\alpha \exp\left[-\left(\frac{\sigma}{\sigma_*}\right)^\beta\right] \times \frac{\beta}{\Gamma(\alpha/\beta)} \frac{d\sigma}{\sigma}, \quad (3)$$

where  $\Gamma$  is the gamma function, and  $dn$  is the differential number of galaxies per unit velocity dispersion per unit comoving volume. Thus for the lens velocity dispersion distribution, we have

$$\sigma \sim \phi(\sigma). \quad (4)$$

We adopt the parameter values Choi et al. (2007) derived from the Sloan Digital Sky Survey (SDSS):  $(\phi_*, \sigma_*, \alpha, \beta) = (8 \times 10^{-3} h^3 \text{ Mpc}^{-3}, 161 \text{ km s}^{-1}, 2.32, 2.67)$ . We assume the mass distribution and velocity function do not evolve with redshift, consistent with the results of Chae (2007), Oguri et al. (2008), and Bezanson et al. (2011). Following Collett (2015), we draw the lens ellipticity from a velocity dispersion-dependent Rayleigh density:

$$e|\sigma \sim \frac{e}{s^2} \exp\left(-\frac{e^2}{s^2}\right), \quad (5)$$

where the scale parameter  $s = A + B\sigma$ , and the fit values are  $A = 0.38$  and  $B = 5.7 \times 10^{-4} (\text{km s}^{-1})^{-1}$ . To exclude highly flattened mass profiles, we truncate the distribution at  $e = 0.8$ . We assume the deflectors have a random orientation, so for the position angle  $\theta_e$  distribution, we have

$$\theta_e \sim U[0, 2\pi]. \quad (6)$$

We simulate the effect of lensing by line-of-sight structures as an external shear term in the deflection potential (e.g., Kochanek 1991; Keeton et al. 1997; Witt & Mao 1997). The deflection potential  $\psi$  of the external shear is given by

$$\psi(x, y) = \frac{\gamma}{2}(x^2 - y^2)\cos 2\theta_\gamma + \gamma xy \sin 2\theta_\gamma, \quad (7)$$

where  $\gamma$  is the magnitude of the shear, and  $\theta_\gamma$  describes its orientation in the image plane. We assume the shear has a random orientation and a Rayleigh distribution in magnitude with scale parameter  $s = 0.05$  (Wong et al. 2011). Thus the  $\gamma$  distribution is

$$\gamma \sim \frac{\gamma}{s^2} \exp\left(-\frac{\gamma^2}{s^2}\right), \quad (8)$$

with  $s = 0.05$ . As the shear orientation is assumed to be random, the  $\theta_\gamma$  distribution is

$$\theta_\gamma \sim U[0, 2\pi]. \quad (9)$$

The lens redshift distribution can be derived from Equation (3), which gives the differential number of galaxies per unit velocity dispersion per unit comoving volume. We begin with the definition of the comoving volume element,

$$dV_C = D_H \frac{(1 + z_l)^2 D_l^2}{E(z_l)} dz_l d\Omega, \quad (10)$$

where  $D_H = c/H_0$  is the Hubble distance,  $E(z_l) = \sqrt{\Omega_M(1 + z_l)^3 + \Omega_\Lambda}$  in our assumed cosmology, and  $D_l$  is the angular diameter distance to the lens. Since  $dn = dn/dV_C$ , we can combine Equation (3) with Equation (10) to derive the unnormalized, all-sky ( $d\Omega = 4\pi$ ) redshift and velocity dispersion function:

$$\frac{dN}{d\sigma dz_l} = 4\pi D_H \frac{(1 + z_l)^2 D_l^2}{E(z_l)} \phi(\sigma). \quad (11)$$

As  $\phi(\sigma)$  has no dependence on  $z_l$ , we can marginalize  $\sigma$  out of Equation (11) and drop constants to obtain an unnormalized density for  $z_l$ :

$$\frac{dN}{dz_l} \propto \frac{(1 + z_l)^2 D_l^2}{E(z_l)}. \quad (12)$$

We normalize Equation (12) by a constant,  $K$ :

$$K = \int_{z_{l,\min}}^{z_{l,\max}} \frac{(1+z_l)^2 D_l^2}{E(z_l)} dz_l, \quad (13)$$

where  $z_{l,\min}$  and  $z_{l,\max}$  are the minimum and maximum lens redshifts considered in the simulation, respectively. We combine Equations (12) and (13) to obtain the probability density function for  $z_l$ :

$$p(z_l) = \frac{1}{K} \frac{(1+z_l)^2 D_l^2}{E(z_l)}. \quad (14)$$

Finally, as a matter of convention, we always take the SIE mass profile centroid coordinates  $x_l$  and  $y_l$  to be

$$x_l = 0, \quad (15)$$

$$y_l = 0. \quad (16)$$

With sampling prescriptions for  $e$ ,  $\gamma$ ,  $\theta_\gamma$ ,  $\sigma$ ,  $z_l$ ,  $x_l$ ,  $y_l$ , and  $\theta_e$ , we can realize deflectors at random.

## 2.2. Lens Galaxies

We use the fundamental plane (Djorgovski & Davis 1987), a canonical relation between the mass, size, and brightness of elliptical galaxies, to assign light profiles to lens galaxies. Throughout this section, we assume the variables  $e$ ,  $\gamma$ ,  $\theta_\gamma$ ,  $\sigma$ ,  $z_l$ ,  $x_l$ ,  $y_l$ , and  $\theta_e$  have already been sampled as described in Section 2.1. As an ansatz, we model the lens galaxy light profiles as Sérsic functions with  $n = 4$  (Sérsic 1963). Such profiles have shown excellent agreement with observations of ellipticals (Lackner & Gunn 2012). Section 2.4 includes a more detailed discussion of Sérsic functions, but for now it is only important that they are specified by seven parameters: an amplitude  $I_e$ , a size parameter  $R_e$ , a shape parameter  $n$ , a centroid position (here  $x'_l$  and  $y'_l$ ), an ellipticity (here  $e'$ ), and a position angle (here  $\theta'_e$ ). The spectra of elliptical galaxies are remarkably uniform, with the primary feature being the break at 4000 Å (rest frame). Therefore, we model the spectral energy distributions (SEDs) of the lens light profiles using the one-component Elliptical template of Kinney et al. (1996). We assume that the ellipticities and position angles of the lens light profiles are the same as those of their corresponding mass profiles, in other words, that the light traces the mass. Therefore, for the lens galaxy light profile position angle  $\theta'_e$ , the lens galaxy light profile ellipticity  $e'$ , and the lens galaxy light profile centroid coordinates  $x'_l$  and  $y'_l$ , we have

$$\theta'_e = \theta_e, \quad (17)$$

$$e' = e, \quad (18)$$

$$x'_l = x_l, \quad (19)$$

$$y'_l = y_l. \quad (20)$$

Bernardi et al. (2003) express the fundamental plane as a multivariate normal relationship between the velocity dispersion  $\sigma$ , the surface brightness  $\mu$ , and the effective radius  $R_e$ :

$$\begin{bmatrix} \mu \\ R \\ V \end{bmatrix} \sim \mathcal{N} \left( \begin{bmatrix} \mu_{*,c} \\ R_* \\ V_* \end{bmatrix}, \begin{bmatrix} \sigma_\mu^2 & \sigma_R \sigma_\mu \rho_{R\mu} & \sigma_V \sigma_\mu \rho_{V\mu} \\ \sigma_R \sigma_\mu \rho_{R\mu} & \sigma_R^2 & \sigma_R \sigma_V \rho_{RV} \\ \sigma_V \sigma_\mu \rho_{V\mu} & \sigma_R \sigma_V \rho_{RV} & \sigma_V^2 \end{bmatrix} \right), \quad (21)$$

where  $V \equiv \log(\sigma/[1 \text{ km s}^{-1}])$ ,  $R \equiv \log(R_e/[1 h_{70} \text{ km}])$ , and  $\mu_{*,c}$  is a  $k$ -corrected  $\mu_*$  defined by a correction factor  $Q$ :

$$\mu_{*,c} = \mu_* - Q z_l. \quad (22)$$

Fitting the model to the  $i^*$ -band photometry of a sample of roughly 9000 early-type galaxies from SDSS, Bernardi et al. (2003) find  $\sigma_\mu = 0.600$ ,  $\mu_* = 19.40$ ,  $R_* = 0.465$ ,  $\sigma_R = 0.241$ ,  $V_* = 2.201$ ,  $\sigma_V = 0.110$ ,  $\rho_{R\mu} = 0.753$ ,  $\rho_{V\mu} = -0.001$ ,  $\rho_{RV} = 0.542$ , and  $Q = 0.75$ . We adopt these values in our simulations.

Using a conditioning identity for multivariate Gaussians,<sup>6</sup> we can rewrite Equation (21) to obtain the joint distribution of  $\mu$  and  $R$ :

$$\begin{bmatrix} \mu \\ R \end{bmatrix} | V \sim \mathcal{N} \left( \begin{bmatrix} V - V_* \\ R_* + \sigma_R \rho_{RV} \end{bmatrix}, \begin{bmatrix} \sigma_\mu^2 (1 - \rho_{V\mu}^2) & \sigma_R \sigma_\mu (\rho_{R\mu} - \rho_{RV} \rho_{V\mu}) \\ \sigma_R \sigma_\mu (\rho_{R\mu} - \rho_{RV} \rho_{V\mu}) & \sigma_R^2 (1 - \rho_{RV}^2) \end{bmatrix} \right). \quad (23)$$

Using Equation (23), we sample  $\mu$ ,  $R$  pairs given the velocity dispersion  $\sigma$ . We then convert  $\mu$  into an  $i$ -band apparent AB magnitude  $m_i$  using the following relation from Bernardi et al. (2003):

$$\begin{aligned} m_i = \mu &- 5 \log \left( \frac{R_e/D_l}{1''} \right) - 2.5 \log(2\pi) \\ &+ 10 \log(1+z_l). \end{aligned} \quad (24)$$

We then linearly rescale the flux of the Elliptical template so that its  $i$ -band apparent magnitude is  $m_i$ . We assume that the spectrum of the galaxy is spatially constant, so  $m_i$  also fixes  $I_e$ . With the results of Section 2.1 and sampling prescriptions for  $m_i$ ,  $R_e$ ,  $\theta'_e$ ,  $e'$ ,  $x'_l$ , and  $y'_l$ , we can realize lens galaxy light profiles at random.

In our model of the lens galaxy population, we neglect microlensing by lens galaxy stars. Studies have shown that microlensing can cause significant errors when using gLSNe to measure time delays (Dobler & Keeton 2006; Goldstein et al. 2018) or constrain mass models (Foxley-Marrable et al. 2018). However, the effect of microlensing on gLSN yields has been shown to be small (Goldstein et al. 2018).

## 2.3. Supernovae

We consider seven different supernova subtypes in this analysis: Type Ia, Type IIP, Type IIn, Type IIL, Type Ib/c, SN 1991bg-like, and SN 1991T-like supernovae. Type Ia, SN 1991bg-like, and SN 1991T-like supernovae are believed to result from the thermonuclear explosions of white dwarfs (Maoz et al. 2014), whereas SNe IIP, SNe IIL, SNe Ib/c, and SNe IIn result from core collapse in massive stars. Our model of the supernova population is characterized by two global parameters for each supernova subtype: a mean peak rest-frame  $B$ -band absolute magnitude in the Vega system  $\mu_{M_B}$ , and the scatter in this magnitude  $\sigma_{M_B}$ . Throughout this section, we assume that deflector and lens galaxy parameters have already been sampled as described in Sections 2.1 and 2.2. For each supernova in the simulation, we realize a peak rest-frame

<sup>6</sup> <https://cs.nyu.edu/~roweis/notes/gaussid.pdf>, Equation 5(d).

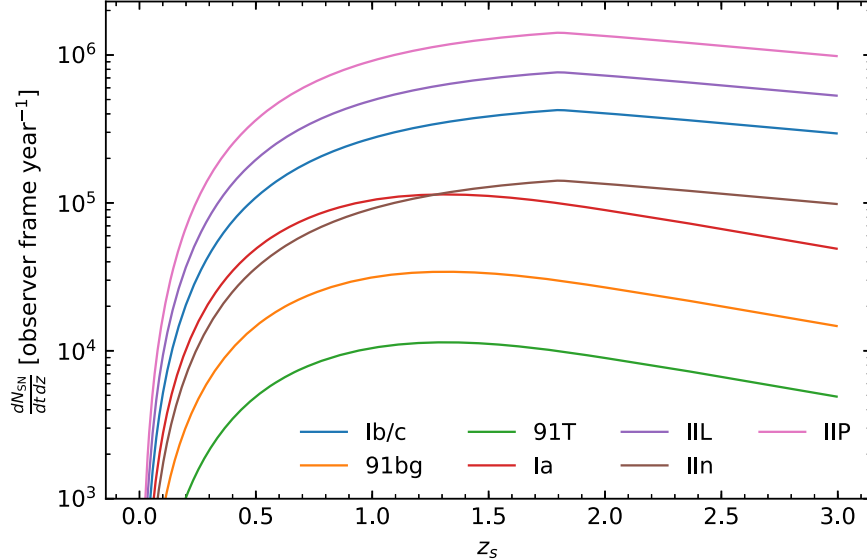


**Figure 1.** All-sky supernova rates as a function of redshift (observer frame). In our simulations, supernova redshifts are realized at random from these distributions. The references in Table 1 provide the data sources of these curves.

**Table 1**  
Details of the Supernova Population Model

SN Type	$\mu_{M_B}$	$\sigma_{M_B}$	Template	Template References	Luminosity and Rate References
IIP	-16.9	1.12	SN 2005lc	Sako et al. (2011)	Li et al. (2011)
91bg	-17.15	0.2	Nugent-91bg	Nugent et al. (2002)	Sullivan et al. (2006)
Ia	-19.23	0.1	Hsiao v3.0	Hsiao et al. (2007)	Sullivan et al. (2006)
91T	-19.3	0.2	Nugent-91T	Nugent et al. (2002)	Sullivan et al. (2006)
III	-17.46	0.38	Nugent-III	Gilliland et al. (1999)	Li et al. (2011)
IIIn	-19.05	0.5	Nugent-IIIn	Gilliland et al. (1999)	Li et al. (2011)
Ibc	-17.51	0.74	Nugent-Ibc	Levan et al. (2005)	Li et al. (2011)

**Note.** Magnitudes are given in the Vega system.

B-band absolute magnitude  $M_B$  according to

$$M_B \sim \mathcal{N}(\mu_{M_B}, \sigma_{M_B}). \quad (25)$$

In our Monte Carlo simulation, we randomly draw the unlensed angular position of each supernova uniformly over a circular area of angular radius  $\theta_l$  centered on the lens galaxy. Using another Monte Carlo simulation, we found that in more than 99.9% of cases, multiply imaged point sources had unlensed positions within  $0.9\theta_E$  of the SIE centroid. Therefore, in the present calculations, we set  $\theta_l = 0.9\theta_E$ , where  $\theta_E$  is the lens's angular Einstein radius, which can be calculated via Equation (2). To realize random supernova positions uniformly over this area, we first draw two random deviates from the uniform distribution,

$$r \sim U[0, 1], \quad (26)$$

$$\theta \sim U[0, 2\pi], \quad (27)$$

then convert these into lens-centered Euclidean angular coordinates  $x_s$  and  $y_s$  via

$$x_s = \theta_l \sqrt{r} \cos \theta, \quad (28)$$

$$y_s = \theta_l \sqrt{r} \sin \theta. \quad (29)$$

This ensures that supernovae are realized uniformly over each lens's area of influence. We draw a redshift for each supernova

from the functions  $f_T(z_s)$  shown in Figure 1. The normalized Figure 1 curves  $S_T(z_s)$  give the redshift probability density function for supernova type  $T$ ,

$$p(z_s) = S_T(z_s), \quad (30)$$

where  $z_s$  is the source redshift. For each supernova subtype, we assume that the spectral evolution is described by a template with one parameter (the overall normalization), and we use the realized  $M_B$  to set its value assuming the Planck Collaboration et al. (2016) cosmology described in Section 1. With sampling prescriptions for  $M_B$ ,  $z_s$ ,  $x_s$ , and  $y_s$ , we can realize supernovae at random. Table 1 lists the references for our supernova templates, rates, and luminosity functions.

The supernova rate curves shown in Figure 1 were obtained by fixing theoretical models of the supernova rate to actual supernova rate measurements at fiducial redshifts. In the present calculations, we assume that the redshift-dependent core-collapse supernova rate (used above for SNe IIP, III, IIIn, and Ib/c) is directly proportional to the cosmic star formation rate. We make this assumption because the delay time between the formation and death of stars that explode as core-collapse supernovae (in megayears) is much smaller than the characteristic timescale over which the star formation rate evolves (gigayears). The redshift-dependent thermonuclear supernova rate is taken to follow the SFH-II model of Pain et al. (2002).

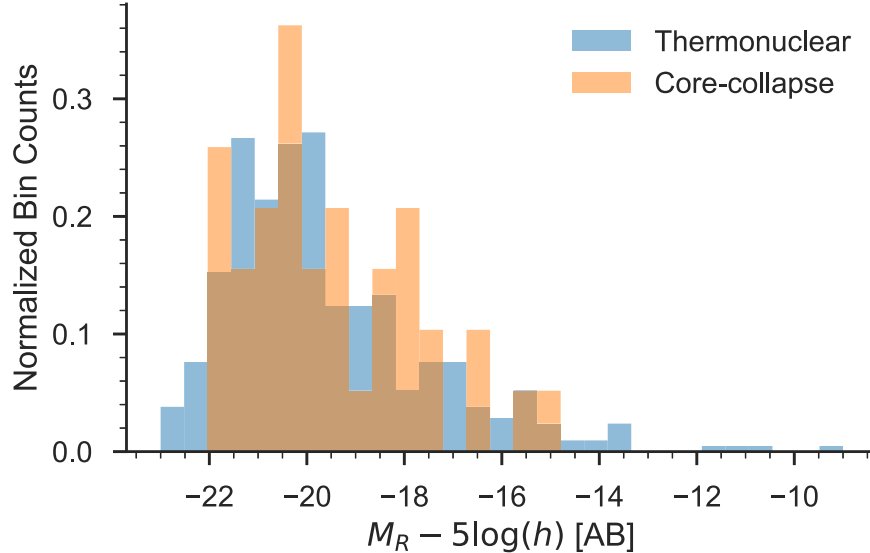


**Figure 2.** Host galaxy luminosity functions used in our simulations.

These curves are normalized to the core-collapse and thermonuclear rate measurements at fiducial redshifts from the references in Table 1, with the relative breakdown of supernova subtypes taken from Richardson et al. (2014). Although the redshift dependence of the supernova rate is well constrained on observational and theoretical grounds, the overall normalization of the supernova rate is associated with significant uncertainty, at the level of tens of percent. For example, Bazin et al. (2009) measured the core-collapse supernova rate at  $z \approx 0.3$  with an uncertainty of roughly 30%. As the yields we present in Section 3 are linearly dependent on the overall normalization of the supernova rate (see Section 2.10), and because this is the dominant uncertainty in our analysis, our yields should be taken to be uncertain by approximately this factor.

#### 2.4. Host Galaxies

The connection between supernovae and their host galaxies is of critical importance to time-delay cosmology with gLSNe, as lensed host galaxy arcs will provide significant leverage on lens models (e.g., Suyu et al. 2017). Here we describe an empirical model of the supernova–host galaxy connection that we use to realize hosts for each supernova in our simulation. Throughout this section, we assume that deflector, lens galaxy, and supernova parameters have already been sampled as described in Sections 2.1–2.3. We consider three types of host galaxies: elliptical galaxies, which have almost no ongoing star formation, S0/a-Sb galaxies, which have a moderate level of ongoing star formation, and late-type/spiral galaxies, which have vigorous ongoing star formation. As an ansatz, we take the light profiles of the host galaxies in the absence of lensing to be Sérsic functions with  $n = \{1, 1, 4\}$ , respectively. Only normal SNe Ia and SN 1991bg-like events have been observed to be hosted by elliptical or S0/a-Sb galaxies. Based on measured rates, we assume these two subclasses of thermonuclear supernovae have a 30% chance of being hosted by an elliptical, a 35% chance of being hosted by an S0/a-Sb, and a 35% chance of being hosted by a late-type/spiral, roughly consistent with the results of Han et al. (2010), Li et al. (2011), Hakobyan et al. (2012), and Smith et al. (2012). In our

simulations, Type Ib/c, Type IIP, Type IIL, Type IIn, and SN 1991T-like supernovae can only be hosted by late-type/spiral galaxies. For simplicity, we assume the spectra of the host galaxies are given by the following Kinney et al. (1996) templates: Elliptical (elliptical), SC (S0/a-Sb), and Starburst (late-type/spiral).

We draw the host galaxy luminosities from two separate luminosity functions: one for the hosts of thermonuclear supernovae (SNe Ia, SN 1991bg-like, and SN 1991T-like events) and one for the hosts of core-collapse supernovae. We construct both of our luminosity functions using supernovae discovered by the Palomar Transient Factory (PTF; Law et al. 2009). PTF discovered thousands of supernovae to  $z \sim 0.1$  and obtained spectral confirmation of many of them in a relatively unbiased manner. For the core-collapse supernovae, we draw the cosmology-independent host galaxy rest-frame  $R$ -band absolute magnitude  $M_R - 5 \log h$  at random from the sample of Arcavi et al. (2010) confined to  $0.01 \leq z \leq 0.05$  to limit the effects of peculiar velocities and to ensure a complete sample. For the thermonuclear events, we use a catalog compiled by E. Y. Hsiao & P. E. Nugent (2019, private communication) drawn from the PTF discoveries that overlapped with fields observed by SDSS and the Baryon Oscillation Spectroscopic Survey.

Figure 2 shows the luminosity functions of core-collapse and thermonuclear supernova host galaxies used in the present calculations. The host galaxy redshift  $z'_s$  is fixed to the redshift of the supernova

$$z'_s = z_s. \quad (31)$$

The sampled values of  $M_R - 5 \log h$  and  $z'_s$  fix the normalization of the host galaxy spectral template and the host galaxy Sérsic profile amplitude under the assumption of a Planck Collaboration et al. (2016) cosmology.

Following Shen et al. (2003), we take the sizes and intrinsic brightnesses of galaxies to be correlated via the “size-luminosity relation”

$$p(\log R'_e | M_R) = \mathcal{N}(\log \bar{R}_e, \sigma_{\log R_e}), \quad (32)$$

where  $R'_e$  is the effective radius of the host galaxy Sérsic profile, and  $\bar{R}_e$  and  $\sigma_{\log R_e}$  are global parameters. Shen et al. (2003) find

that for elliptical galaxies,  $R'_e$  is related to  $M_R$  via

$$\log\left(\frac{\bar{R}_e}{1 \text{ kpc}}\right) = -0.4aM_{R,c} + b, \quad (33)$$

where

$$M_{R,c} = M_R + 5 \log\left(\frac{0.7}{h}\right). \quad (34)$$

Fitting to data from SDSS, Shen et al. (2003) find  $a = 0.65$  and  $b = -5.06$ . For S0/a-b and late-type/spiral galaxies, they find

$$\begin{aligned} \log\left(\frac{\bar{R}_e}{1 \text{ kpc}}\right) &= -0.4\alpha M_{R,c} + (\beta - \alpha) \\ &\times \log[1 + 10^{-0.4(M_{R,c} - M_0)}] + \gamma, \end{aligned} \quad (35)$$

where fitting the SDSS data give  $\alpha = 0.26$ ,  $\beta = 0.51$ ,  $\gamma = -1.71$ , and  $M_0 = -20.91$ . The dispersion in the size-luminosity relation is given by

$$\sigma_{\log R_e} = \sigma_2 + \frac{(\sigma_1 - \sigma_2)}{1 + 10^{-0.8(M_{R,c} - M_0)}} \quad (36)$$

for all galaxy types, with  $\sigma_1 = 0.45$  and  $\sigma_2 = 0.27$ . Having calculated  $\sigma_{\log R_e}$  and  $\bar{R}_e$  given  $M_R$ , we can sample a value of  $\log R'_e$  using Equation (32).

The next steps are to draw the host galaxy ellipticity  $e''$  and position angle  $\theta''_e$ . We take the host galaxy orientation to be random,

$$\theta''_e \sim U[0, 2\pi], \quad (37)$$

and to draw ellipticities, we use the results of the Cosmic Evolution Survey (COSMOS; Scoville et al. 2007). COSMOS is a survey designed to probe the correlated evolution of galaxies, star formation, active galactic nuclei, and dark matter with large-scale structure. Our access point to COSMOS is the Advanced Camera for Surveys General Catalog (ACS-GC; Griffith et al. 2012). ACS-GC is a photometric and morphological database containing fits of structural parameters to publicly available data obtained with the ACS instrument on board *Hubble Space Telescope* (*HST*). The catalog was created using the code Galapagos (Häubler et al. 2007, 2011), which incorporates the source extraction and photometry software SExtractor (Bertin & Arnouts 1996) and the galaxy light profile fitting algorithm GALFIT (Peng et al. 2002). ACS-GC contains photometry and structural parameters for approximately 305,000 objects (both compact and extended) from COSMOS. The COSMOS images were taken with the Wide Field Camera (WFC) on ACS, through the F814W filter, a broad *i*-band filter spanning the wavelength range 7000–9600 Å, with a scale of 0.05 arcsec pixel<sup>-1</sup> and a resolution of 0''.09 FWHM.

We apply the cuts of Gupta et al. (2016) to create a list of potential supernova host galaxies from the ACS-GC. We further subdivide this list into two groups: “early”- and “late”-type galaxies, having fitted values of the Sérsic index in the ACS-GC of  $n > 2.5$  and  $n \leq 2.5$ , respectively. For elliptical hosts, we draw  $e''$  at random from the fitted ellipticity values of the “early” group, and for S0/a-b and late-type/spiral hosts, we draw  $e''$  at random from the fitted ellipticity values of the “late”-type group.

The last parameters to draw are the unlensed coordinates of the host galaxy centroid  $x_h$  and  $y_h$ . Here we take the probability density function (PDF) of supernova positions within the host galaxy to be directly proportional to the light profile, an assumption that has been borne out by observational studies that show supernova positions follow host light (e.g., Kelly & Kirshner 2012). Thus we sample offsets  $\Delta x$  and  $\Delta y$  at random from the host galaxy light profile, and then take

$$x_h = x_s - \Delta x, \quad (38)$$

$$y_h = y_s - \Delta y. \quad (39)$$

The host galaxy light profiles follow a Sérsic function, defined as

$$I(r_c) = I_e \exp\left\{-b_n\left[\left(\frac{r_c}{R_e}\right)^{\frac{1}{n}} - 1\right]\right\}, \quad (40)$$

where  $r_c$  is an ellipticity-free, host-galaxy-centered radial coordinate, and  $b_n$  is a constant scalar solution to the equation

$$\gamma(2n; b_n) = \frac{1}{2}\Gamma(2n), \quad (41)$$

in which  $\Gamma$  is the Gamma function and  $\gamma$  is the incomplete Gamma function.<sup>7</sup> To sample a position at random from the surface brightness profile, we first draw two random deviates  $z$  and  $\theta'$  uniformly:

$$z \sim U[0, 1], \quad (42)$$

$$\theta' \sim U[0, 2\pi]. \quad (43)$$

Using the sampled  $z$ , we solve the following equation<sup>8</sup> for  $x$ :

$$\gamma(2n; x) = z\Gamma(2n), \quad (44)$$

then convert  $x$  into the radial coordinate  $r_c$  (see, e.g., Graham & Driver 2005):

$$r_c = R'_e \left(\frac{x}{b_n}\right)^n. \quad (45)$$

We can now write the ellipticity-free host offsets  $\Delta x_c$  and  $\Delta y_c$  as

$$\Delta x_c = r_c \cos \theta, \quad (46)$$

$$\Delta y_c = r_c \sin \theta. \quad (47)$$

We add ellipticity to obtain  $\Delta x_e$  and  $\Delta y_e$ :

$$\Delta x_e = \Delta x_c \sqrt{1 - e}, \quad (48)$$

$$\Delta y_e = \Delta y_c / \sqrt{1 - e}. \quad (49)$$

Finally, we account for the position angle of the host galaxy  $\theta''_e$  by applying a rotation matrix:

$$\begin{pmatrix} \Delta x \\ \Delta y \end{pmatrix} = \begin{pmatrix} \cos \theta''_e & \sin \theta''_e \\ -\sin \theta''_e & \cos \theta''_e \end{pmatrix}^{-1} \begin{pmatrix} \Delta x_e \\ \Delta y_e \end{pmatrix}. \quad (50)$$

With sampling prescriptions for  $M_R$ ,  $R'_e$ ,  $\theta''_e$ ,  $e''$ ,  $x_h$ , and  $y_h$ , we can realize host galaxy light profiles at random.

<sup>7</sup> An exact, computationally inexpensive method of calculating  $b_n$  for a given value of  $n$  is to evaluate `gammaincinv(2 * n, 0.5)` in `scipy`.

<sup>8</sup> See Footnote 7, but with the substitutions  $b_n \rightarrow x$  and `gammaincinv(2 * n, 0.5) → gammaincinv(2 * n, z)`.

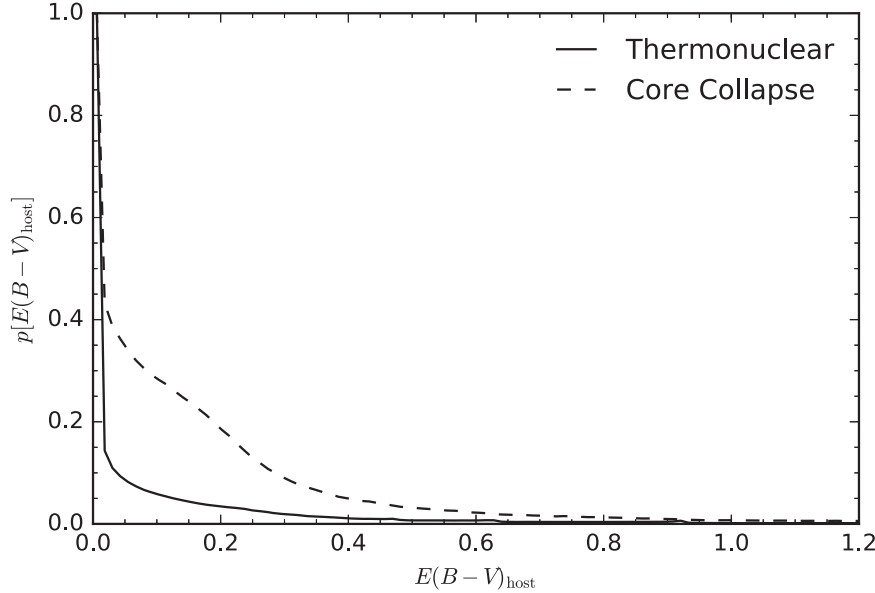


**Figure 3.**  $E(B - V)_{\text{host}}$  distributions for galaxies at random orientations, from Hatano et al. (1998). Host reddenings for Type Ia, SN 1991T-like, and SN 1991bg-like supernovae are drawn from the thermonuclear curve. Host reddenings for SNe IIP, IIL, IIn, and Ib/c are drawn from the core-collapse curve.

### 2.5. Sky Distribution

We assign a sky location to each system realized in our simulation, which in turn determines the sampling, signal-to-noise ratio, and filters of its simulated photometry. The sky location also controls the amount of Milky Way dust extinction each system experiences (see Section 2.6). To randomly assign a sky position to a gLSN system, we draw two random deviates  $u$  and  $v$  uniformly:

$$u \sim U[0, 1], \quad (51)$$

$$v \sim U[0, 1]. \quad (52)$$

We then convert these to equatorial coordinates  $\alpha$  (R.A.) and  $\delta$  (decl.) via

$$\delta = \frac{180^\circ \times \arccos(2v - 1)}{\pi} - 90^\circ \quad (53)$$

and

$$\alpha = 360^\circ \times u. \quad (54)$$

This sampling prescription ensures that systems are distributed uniformly over the celestial sphere.

### 2.6. Extinction

After randomly assigning a sky location to each gLSN system, we use the `sfdmap`<sup>9</sup> implementation of the extinction maps of Schlegel et al. (1998), scaled to the recalibrated values of Schlafly & Finkbeiner (2011), to calculate the associated Milky Way reddening value,  $E(B - V)_{\text{MW}}$ . We then apply the extinction to the observer-frame spectral time series of the supernova images using a Cardelli et al. (1989) reddening law with  $R_V = 3.1$ . In addition to extinction by dust in the Milky Way, gLSNe can suffer extinction by dust in their host galaxies. Here we assume the host galaxy reddening  $E(B - V)_{\text{host}}$  is distributed according to the thermonuclear

and core-collapse extinction distributions of Hatano et al. (1998) for galaxies at random orientations, shown in Figure 3. We apply host extinction to the rest-frame spectral time series of the supernova images using a Cardelli et al. (1989) reddening law with  $R_V = 3.1$ , the measured Galactic value. Amanullah et al. (2015) showed that there is significant diversity in the value of  $R_V$  for the observed host galaxy extinction in SNe Ia, and similar conclusions were reached for certain types of core-collapse SNe in Stritzinger et al. (2018). In particular, lower values of  $R_V$  are often found (see Bulla et al. 2018 for a proposed explanation). By selecting a value of  $R_V$  on the upper range observed, we are assuming a relatively large attenuation by dust,  $A_V = R_V \times E(B - V)$ , that is, a conservative estimate of the SN brightness. We neglect extinction by dust in the lens galaxies, which may reduce yields by making lensed images fainter. iPTF16geu showed evidence of extinction due to lens galaxy dust at subkiloparsec offsets (Goobar et al. 2017), but with only one event, the frequency and spatial distribution of lens galaxy dust remain unclear. ZTF and LSST will be able to better constrain lens galaxy dust extinction by producing large samples of gLSNe Ia.

### 2.7. Simulated Surveys

To simulate realistic light curves and pixel cutouts of our lens systems as they would appear in a survey, we must account for the survey’s unique observing strategy and conditions, instrumental properties, and visit schedule. To do this, we use the outputs of software tools that run survey simulations with given science-driven desirables, a software model of the telescope and its control system, and models of weather and other environmental variables. Such simulations produce observation histories, which are records of times, pointings, and associated environmental data and telescope activities throughout a simulated survey. These histories can be examined to assess whether a simulated survey would be useful for any particular purpose or interest. We adopt a common

<sup>9</sup> <https://github.com/kbarbary/sfdmap>

format for survey observation histories, consisting of a table with the following columns:

1. `field`: Field ID of the observation.
2. `filter`: Filter in which the observation was taken.
3. `time`: MJD at which the observation began (the shutter-open time).
4. `exptime`: Integration time of the exposure.
5. `sky_counts_per_pixel`: Sky counts (in electrons) in each pixel. This is not a count rate, but the counts integrated over the entire exposure. This column can optionally also include counts due to other spatially uniform Poisson backgrounds, such as dark current.
6. `psf_sigma`: Standard deviation (in arcseconds) of the point-spread function (PSF), modeled as a Gaussian.
7. `ra`: R.A. of the center of the pointing.
8. `dec`: decl. of the center of the pointing.
9. `night` (optional): Integer ID specifying the night of the survey in which the observation was taken, used for grouping and stacking observations.

In addition to the observation histories, we specify instrumental properties with the following parameters:

1. `pix_scale`: Plate scale of the camera (arcsec/pixel).
2. `read_noise`: Read noise of the camera, in electrons.
3. `field_of_view`: Field of view of the imager, in deg<sup>2</sup>.
4. `collecting_area`: Collecting area of the telescope, in cm<sup>2</sup>.

In this work, we consider two surveys, ZTF and LSST, the two largest imaging surveys at optical wavelengths during the periods 2018–2021 and 2021–2032, respectively. In the following subsections, we describe these surveys and the operations simulations that we use to realize their data.

### 2.7.1. The Zwicky Transient Facility

ZTF is an ongoing time-domain imaging survey observing a minimum of 15,000 deg<sup>2</sup> in the *g* and *r* bands ( $\delta > -30^\circ$ ) every three nights to a median depth of 20.5 mag, with transient alerts released in real time to the public.<sup>10</sup> In 2018 March, ZTF began science operations, replacing its predecessor, the intermediate Palomar Transient Factory (iPTF), on the 1.2 m Oschin-Schmidt telescope (P48) at Palomar Observatory near San Diego, California. The chief advance of ZTF over iPTF is a new wide-field camera developed for the survey (Smith et al. 2014; Bell et al. 2018). With its 47 deg<sup>2</sup> field of view, the ZTF camera can survey 3750 deg<sup>2</sup> per hour, making it roughly an order of magnitude faster than iPTF. In addition to the 15,000 deg<sup>2</sup> public survey, a subset of 1600 deg<sup>2</sup> is currently monitored three times per night in two filters as a part of the ZTF partnership survey. Half of the survey area is also monitored in the *i* band every four nights. The remaining 20% of the survey time is allocated to proposals from collaboration members affiliated with the California Institute of Technology (Caltech) on a competitive basis. We simulate data from all three ZTF programs in the present work using the simulated ZTF survey of Bellm et al. (2019), which uses the same scheduler as the actual survey. The scheduler uses Gurobi optimization,<sup>11</sup> a technique for integer programming, to maximize the number of images, weighted by the volume

<sup>10</sup> Public alerts can be retrieved from <http://ztf.uw.edu>.

<sup>11</sup> <http://www.gurobi.com/>

surveyed per image, observed in acceptable cadence windows, while maintaining a balance between the public, partnership, and Caltech surveys. While the observing sequence determined by the scheduler in the simulation is reliable, the observing conditions used by the simulation are overly optimistic, predicting limiting magnitudes of  $\sim 21.5$  in all filters. In reality, ZTF can only reach a limiting magnitude of 20.5 in any filter in a 30 s exposure. Therefore, in our simulation, we set the seeing FWHM to 2'', the survey median, and the limiting magnitude ( $5\sigma$ ) to 20.5 for all observations.

### 2.7.2. The Large Synoptic Survey Telescope

LSST is a planned imaging experiment that will conduct at least two interleaved surveys: a “wide-fast-deep” (WFD) survey covering roughly 20,000 deg<sup>2</sup> in *ugrizy* every two to three weeks with 30 s exposures ( $r_{\text{lim}} \sim 24$ ), and a “deep-drilling” survey covering a smaller area at a significantly higher cadence (LSST Science Collaboration et al. 2017). A new 8 m telescope and camera with a 9.6 deg<sup>2</sup> field of view and 0''.2 pixels, located on the Cerro Pachón ridge in northern Chile, are currently under construction to carry out the survey. First light and commissioning operations will begin in 2021, followed by science operations in 2022. The survey will collect data for 10 yr.

Several candidate observing strategies have been proposed for LSST. In this analysis, we evaluate two of the major ones from the perspective of gLSN science: a nominal observing strategy, known as `minion_1016`, and a leading alternative, known as `altsched`. `minion_1016` divides its time between five interleaved surveys: a “universal” WFD survey (85.1%), a proposal to monitor the North Ecliptic Spur (6.5%), a proposal to monitor the Galactic plane (1.7%), a proposal to monitor the South Celestial Pole (2.2%), and a proposal to monitor five 9.6 deg<sup>2</sup> “deep-drilling” fields (4.5%). The median effective seeing (FWHM) for all proposals in the *r* band is 0''.93. The median single-visit depths for the WFD fields are (23.14, 24.47, 24.16, 23.40, 22.23, 21.57) in the *ugrizy* bands.

The `minion_1016` simulation was performed using the software tool OpSim (Delgado et al. 2014). OpSim uses a greedy algorithm that chooses the best observation at a given time (according to a merit function based on the input science goals), with no look-ahead or long-term strategy. `altsched`, on the other hand, takes a simpler approach, following a preprogrammed path with no merit function. `altsched` attempts to observe fields at low air mass by observing only on the meridian, optimizing the signal-to-noise ratio of the observations. Like `minion_1016`, `altsched` retains a dual visit per night requirement for transient artifact rejection and asteroid orbit linkage, but the two visits are taken in different filters, so colors can be obtained on all objects. `altsched` simulations of SN Ia light curves have shown that the alternative cadence can lead to significantly better light curve sampling than `minion_1016`. In Section 4, we evaluate both `minion_1016` and `altsched` for the LSST gLSN science case.

## 2.8. Imaging, Photometry, and Calibration

To realize images and photometry of our simulated gLSN systems as they would appear in the mock surveys described in Section 2.7, we have developed an image-simulation pipeline based on the open-source astronomical image simulation code

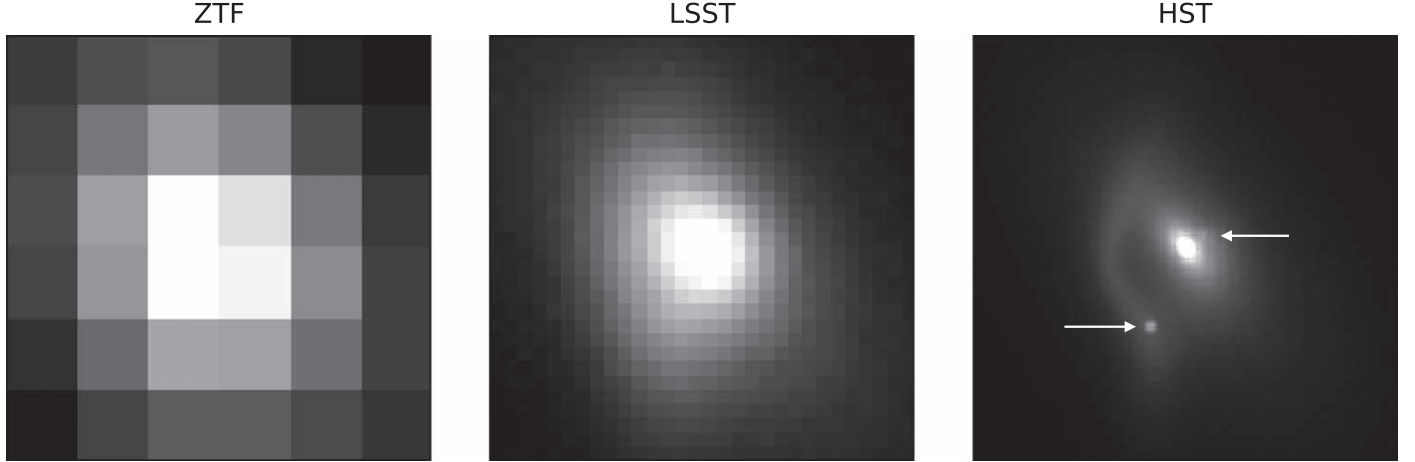


**Figure 4.** Simulated  $r$ -band images of the same gLSN, taken at the same epoch, with three different instruments: ZTF (30 s integration), LSST (30 s integration), and *HST* (one orbit integration through F625W on WFC3). Each panel is  $6'' \times 6''$ . Only in the *HST* data can the resolved images of the transient be clearly seen; they are marked with arrows. ZTF and LSST will be unable to resolve the multiple images of most gLSNe, meaning high-resolution follow-up observations will be critical for lens modeling and time-delay extraction.

GalSim (Rowe et al. 2015) and the gravitational lensing code glafic (Oguri 2010). For a given arrangement of supernova, host galaxy, and lens, we first solve the lens equation using glafic to determine the magnifications, time delays, multiplicities, and locations of the lensed supernova images. We then use glafic to solve the lens equation again for the magnification and surface brightness profile of the lensed host galaxy. With this information, we use GalSim to model the entire system. In GalSim parlance, we model each lensed supernova image as a DeltaFunction, the lens galaxy as a Sérsic, and the lensed host galaxy surface brightness profiles as InterpolatedImages. We convolve the model with a Gaussian model of the PSF, the width of which is provided by the survey simulation (see Section 2.7). We refer to the noiseless convolved model as  $I(x, y)$  and the pixel values of the corresponding model image as  $I_{xy}$ . To generate an image for viewing, we add CCDNoise to the model consisting of Gaussian read noise, Poisson sky background, and Poisson source noise.

We perform photometry using a matched filter, following Bridle et al. (2009). We assume we have a filter  $w_{xy}$  that perfectly matches the shape of the source and is normalized to 1:  $w_{xy} = I_{xy}/\sum I_{xy}$ . We calculate the measured signal as a weighted sum of the image and the filter, via

$$S = \sum_{x,y} w_{xy} I_{xy}, \quad (55)$$

and we define the noise as the square root of the signal variance,

$$N = \sqrt{\text{Var}(S)} = \left[ \sum_{x,y} w_{xy}^2 \sigma_{xy}^2 \right]^{1/2}, \quad (56)$$

where

$$\sigma_{xy}^2 = \text{RN}^2 + I_{xy} + B_{xy}. \quad (57)$$

In Equation (57), RN is the read noise per pixel in  $e^-$ , and  $B_{xy}$  is the flux in  $e^-$  from the background (the sky, dark current, and so on) at pixel  $(x, y)$ . Finally, we determine the image zero

point (ZP) via

$$\text{ZP} = 2.5 \log S + m, \quad (58)$$

where  $m$  is the apparent magnitude of the source through some filter in the AB system. Figure 4 shows three example simulated images of the same gLSN system generated using our pipeline, taken with three different instruments under representative observing conditions.

To increase our sensitivity to faint transients, we stack observations taken in the same filter in a single night. For *minion\_1016*, this has the effect of combining the two exposures taken in the same filter in a  $\sim 30$  minute window to reject moving objects into a single observation with a signal-to-noise ratio roughly a factor of  $\sqrt{2}$  larger. For *altsched*, the stacking has no effect, as the strategy performs revisits to reject moving objects in different filters to obtain colors. For ZTF, stacking has no effect on the public data, which has a typical revisit time of 3–4 days in each filter. However, the stacking significantly boosts survey depth in the high-cadence partnership fields and the Caltech survey. In some regions of these proprietary surveys, a single field may be observed as many as six times per night in a single filter, leading to a potential improvement in depth of  $2.5 \log(\sqrt{6}) \approx 1$  mag over the nominal limiting magnitude of 20.5 in all filters. We apply the discovery technique discussed in the next section (Section 2.9) to the stacked, not raw, data.

An important simplification in our simulations is that we treat gLSN images as a single object when performing photometry. The effect of this assumption is that we can realize a single light curve for each gLSN system, the flux of which is the summed flux of the individual images. For ZTF, this is a reasonable assumption, as the large pixels of the detector and the  $2''$  seeing at Palomar Observatory ensure gLSNe cannot be resolved (see Figure 5). For LSST, as Figure 6 shows, this assumption should hold in most cases. For the cases where the assumption does not hold and the multiple images of a gLSN are resolved, the transient can be detected as two or more bright, nearby transients, as proposed by Oguri & Marshall (2010). For simplicity, we also assume perfect image subtractions. The main implication of this assumption is that

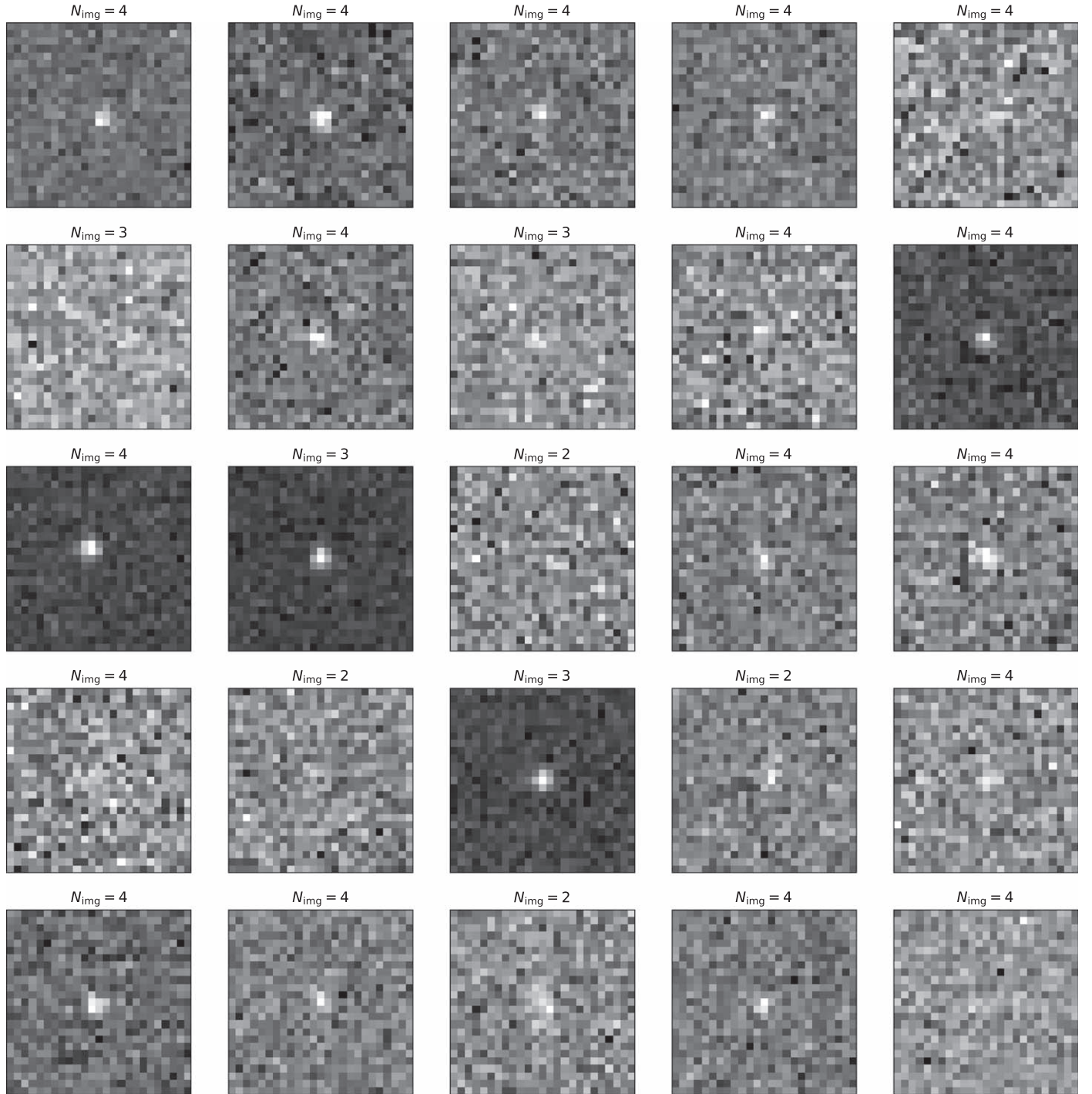


**Figure 5.** Lens-centered difference image cutouts of 25 randomly selected ZTF gLSNe Ia. The difference images are produced by subtracting deep references from science images stacked in 1-day bins. Each cutout is  $25'' \times 25''$ . The sources visible in the cutouts contain flux from the gLSN images only. Lens light and host galaxy light are removed in the subtraction. The low spatial resolution of ZTF ( $1.^{\circ}01$  pixels) combined with the  $2''$  FWHM seeing at Palomar Observatory render the survey unable to resolve multiply imaged supernovae, a feature we exploit in Section 2.9.

photometric accuracy and source detection are unaffected by proximity to the cores of bright lens galaxies. In general, a loss in transient discovery efficiency can be caused by subtraction artifacts near the centers of bright galaxies. Because the point-source saturation limit for ZTF is  $r \sim 12.5$  and the point-source saturation limit for LSST is  $r \sim 16$ , whereas candidate lens galaxies generally have  $r > 18$ , with the nearest ones being spatially extended (and thus having a lower equivalent surface

brightness than their overall magnitude implies), this assumption is reasonable for gLSN searches.

### 2.9. Discovery Technique

We simulate the detection and photometric classification of gLSNe using the technique described in Section 4.1 of Goldstein et al. (2018). The strategy leverages empirical trends to separate

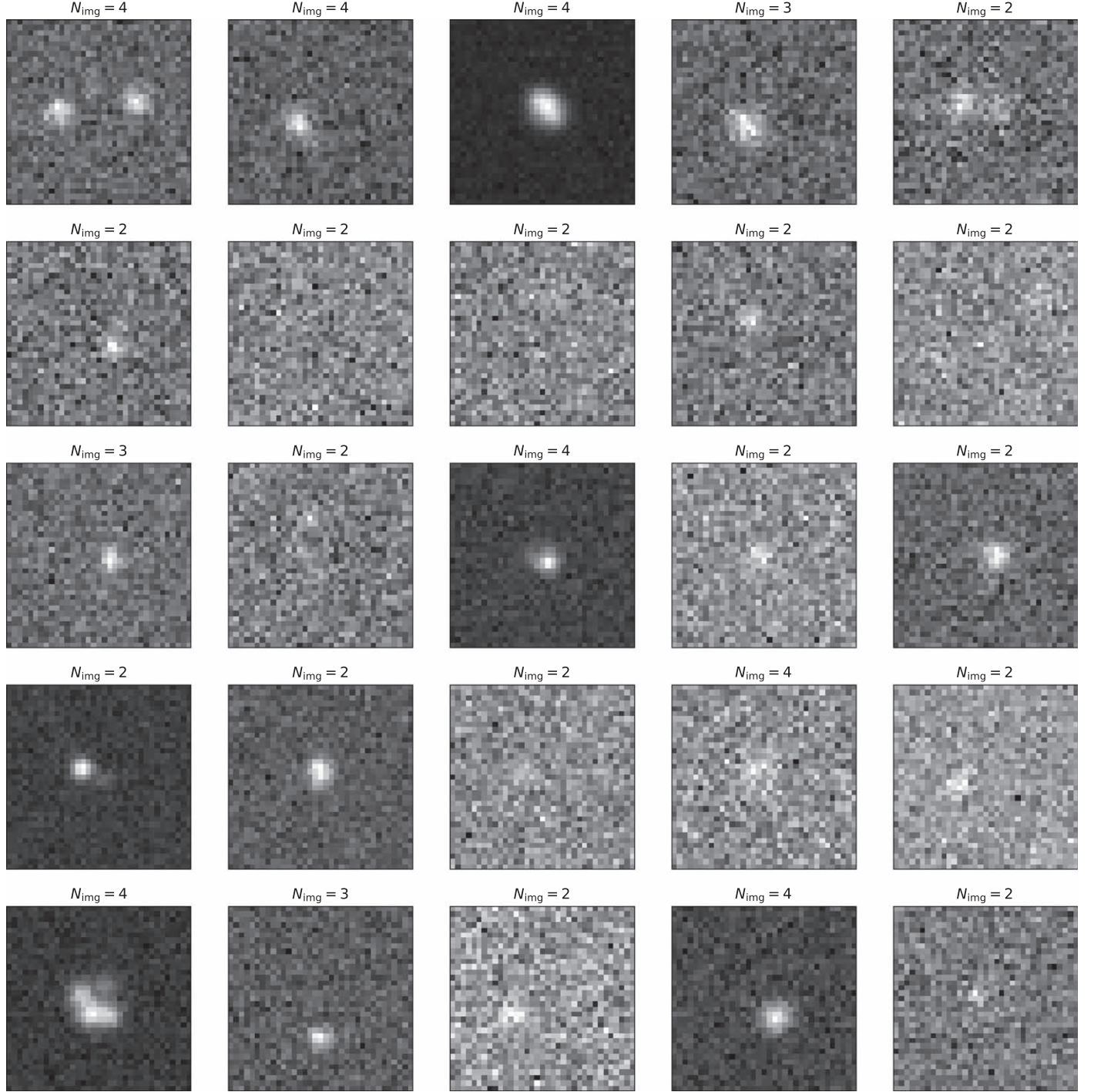


**Figure 6.** Lens-centered difference image cutouts of 25 randomly selected LSST (minion\_1016) gLSNe Ia. Each cutout is  $7'' \times 7''$ . As in Figure 5, the sources visible in the cutouts contain flux from gLSN images only. Lens light and host galaxy light are removed in the subtraction. The improved spatial resolution ( $0''.2$  pixels) of LSST compared to ZTF enables some gLSNe to be totally or marginally resolved, but the majority of systems remain unresolved. LSST must take special care to ensure that its machine learning algorithm for difference image artifact rejection (e.g., Goldstein et al. 2015) does not reject marginally resolved gLSNe, such as the ones in row 5, column 1; row 1, column 4; and row 1, column 5.

gLSNe from other nonlensed transients based on photometric information alone. The strategy can be summarized as follows:

1. Systematically identify supernovae that are spatially coincident with elliptical galaxies (e.g., by cross-matching transient discoveries with an elliptical galaxy catalog).
2. Since elliptical galaxies can only host SNe Ia, test the hypothesis that each supernova actually resides in the elliptical galaxy that appears to be its host by comparing

the brightness, color evolution, and light curve shape of the supernova to those of an SN Ia template at the photometric redshift of the elliptical galaxy.

3. If the supernova is not consistent with being an SN Ia hosted by the elliptical, then it is a candidate for being a lensed supernova at higher redshift.

This technique does not apply to spiral galaxies, because spiral galaxies can host core-collapse supernovae, which have a much

broader range of absolute magnitudes and light curve shapes than SNe Ia.

In the present work, we assume that we have an elliptical galaxy catalog that is complete enough for all supernovae in our simulation to pass the first step in the procedure (i.e., no simulated supernovae are lost because they are lensed by an elliptical galaxy that is not cataloged). This assumption is reasonable in the era of ZTF and LSST, as wide-field multiband imaging surveys such as SDSS and Pan-STARRS have produced relatively complete catalogs of potential lens galaxies out to the redshifts we are interested in ( $z \lesssim 1$ ) in the northern sky. In the era of LSST, elliptical galaxy catalogs with complete photometric redshift coverage will be produced by LSST itself, and by precursor imaging surveys in the south such as the DECam Legacy Survey and the Dark Energy Survey. Additionally, wide-field multiobject spectroscopic surveys such as the Dark Energy Spectroscopic Instrument will greatly increase the redshift completeness of current elliptical galaxy catalogs.

In the present analysis, as in Goldstein et al. (2018), we use the SALT2 SN Ia spectral template (Guy et al. 2007) to perform the second step of the discovery technique. We draw a random reference time  $t_r$  for each gLSN system uniformly over the duration of the survey,

$$t_r \sim U[t_{\min}, t_{\max}], \quad (59)$$

where  $t_{\min}$  and  $t_{\max}$  are the times of the survey's first and last observations, respectively. We realize broadband photometry of each blended gLSN Ia using the technique described in Section 2.8. Starting from the first photometric observation of each gLSN system, we fit the blended light curve with SALT2, fixed to the redshift of the lens galaxy (assumed to be known; see the discussion above). We also enforce bounds on the fit parameters of the SN Ia spectral template; see Section 4 of Goldstein et al. (2018) for further details.

#### 2.10. Importance Sampling, Sample Weighting, and Rate Calculation

We perform a separate Monte Carlo simulation for each survey and supernova type, running each simulation until  $O(10^5)$  gLSN systems are discovered. In each iteration of the simulation, we realize one supernova behind the sampled lens in the lensing area of influence. We run each ZTF simulation for  $N = 10^8$  iterations, and we run each LSST simulation for  $N = 10^7$  iterations. The ZTF simulations require more iterations to converge because ZTF is shallower than LSST, so any given system is less likely to be detected. To reduce shot noise in our results, we use importance sampling to sample lens and source redshifts, the distributions of which contain almost no probability mass in the crucial region  $z \lesssim 0.5$ . Therefore, each system has an associated importance weight factor  $\omega$ :

$$\omega = \frac{f_\Omega p(z_s)p(z_l)}{\mathcal{A} q(z_s)q(z_l)}, \quad (60)$$

where  $p(z_s)$  and  $p(z_l)$  are the true densities of  $z_s$  and  $z_l$  (Equations (14) and (30)),  $q(z_s)$  and  $q(z_l)$  are the sampling densities,  $f_\Omega$  is the ratio of sky area imaged by the survey to the sky area covered in the simulation, and  $\mathcal{A}$  is the factor by which the supernova rate must be multiplied to yield one supernova of the given subtype with  $z_s > z_l$  per year in the

**Table 2**  
gLSN Discovery Rates (in Units of Year $^{-1}$ ) of ZTF and LSST

SN Type	ZTF	LSST (minion_1016)	LSST (altsched)
Type Ia	1.23	47.84	47.42
Type IIP	2.76	88.51	91.06
Type IIn <sup>a</sup>	3.75	209.31	166.54
Type IIL	0.31	11.69	13.10
Type Ib/c	0.36	14.00	16.15
SN 1991bg-like	0.02	0.79	0.89
SN 1991T-like	0.17	5.41	6.09
Total <sup>a</sup>	8.60	380.60	341.27

Note.

<sup>a</sup> Lower limit.

“lensing area of influence” of the lens. We take the sampling densities to be uniform:

$$q(z_s) = U[z_{s,\min}, z_{s,\max}], \quad (61)$$

$$q(z_l) = U[z_{l,\min}, z_{l,\max}], \quad (62)$$

where  $z_{s,\min}$  and  $z_{s,\max}$  are the minimum and maximum supernova redshifts considered in the simulation, respectively. We assume the lenses are uniformly distributed across the sky, so the areal correction factor  $f_\Omega$  can be calculated by dividing the total number of lenses in the survey area by the number of lenses  $N$  realized in the simulation:

$$f_\Omega = \frac{\Omega D_H}{N} \int_{\sigma_{\min}}^{\sigma_{\max}} \phi(\sigma) d\sigma \int_{z_{l,\min}}^{z_{l,\max}} \frac{(1+z_l)^2 D_l^2}{E(z_l)} dz_l, \quad (63)$$

where we have integrated Equation (11) to estimate the total number of lenses in the survey area. In Equation (63),  $\Omega$  is the area of the survey in steradians, and  $\sigma_{\min}$  and  $\sigma_{\max}$  are the minimum and maximum lens velocity dispersions considered in the simulation, respectively.

The number of supernovae per year behind the lens’s area of influence is determined by integrating the observer-frame supernova redshift function (Figure 1) from  $z_l$  or  $z_{s,\min}$  (whichever is larger) to  $z_{s,\max}$  and multiplying by the ratio of the lens’s area of influence to the full-sky area. Taking  $z_1 = \max(z_l, z_{s,\min})$  and  $z_2 = z_{s,\max}$ , we have

$$\mathcal{A} = \left[ \frac{\theta_l^2}{4} \int_{z_1}^{z_2} f_T(z_s) dz_s \right]^{-1}. \quad (64)$$

The weights specify the contribution of a given discovered system to the overall gLSN discovery rate and have units of [year $^{-1}$ ]. The summed weights provide a Monte Carlo estimate of the gLSN discovery rate:

$$\boxed{\sum_{i=0}^N \omega_i = R}, \quad (65)$$

where  $R$  is the total discovery rate (in yr $^{-1}$ ). As with any Monte Carlo estimator, the precision of  $R$  increases as the square root of the number of samples  $N$ . The above scheme is roughly  $10^3$  times more efficient than sampling all of the parameters of the model in a brute-force manner.



**Figure 7.** Model (i.e., noiseless)  $6'' \times 6''$  composite *gri* images of 25 randomly chosen simulated gLSNe, their lens galaxies, and their lensed host galaxies, “detected” by ZTF. Each image is “taken” exactly one night after the transient is detected as a gLSN candidate based on a light curve fit to the simulated ZTF data (see Section 2.9). The FWHM of the seeing on the images is  $0''.1$ , and the pixel scale is  $0''.04$ , identical to that of the UVIS channel of the Wide Field Camera 3 (WFC3) on *HST*.

### 3. Results

Table 2 shows the gLSN discovery rates  $R$  of each simulated survey. Our calculations suggest that under nominal survey operations, ZTF should discover at least 8.60 gLSNe per year, of which at most 4.1% are Type Ib/c, 2.0% are SN 1991T-like, 3.7% are Type IIL, 14.3% are Type Ia, 32.1% are Type IIP, and 0.2% are SN 1991bg-like, and at least 43.6% are Type IIIn. We find that the *minion\_1016* LSST observing strategy should

discover at least 380.60 gLSNe per year, of which at most 12.6% are Type Ia, 1.6% are SN 1991T-like, 23.3% are Type IIP, 4.1% are Type Ib/c, 3.4% are Type IIL, and 0.2% are SN 1991bg-like, and at least 55.0% are Type IIIn. The *altsched* observing strategy should discover at least 341.27 gLSNe per year, of which at most 4.7% are Type Ib/c, 3.8% are Type IIL, 13.9% are Type Ia, 26.7% are Type IIP, 1.8% are SN 1991T-like, and 0.3% are SN 1991bg-like, and at least 45.3% are Type

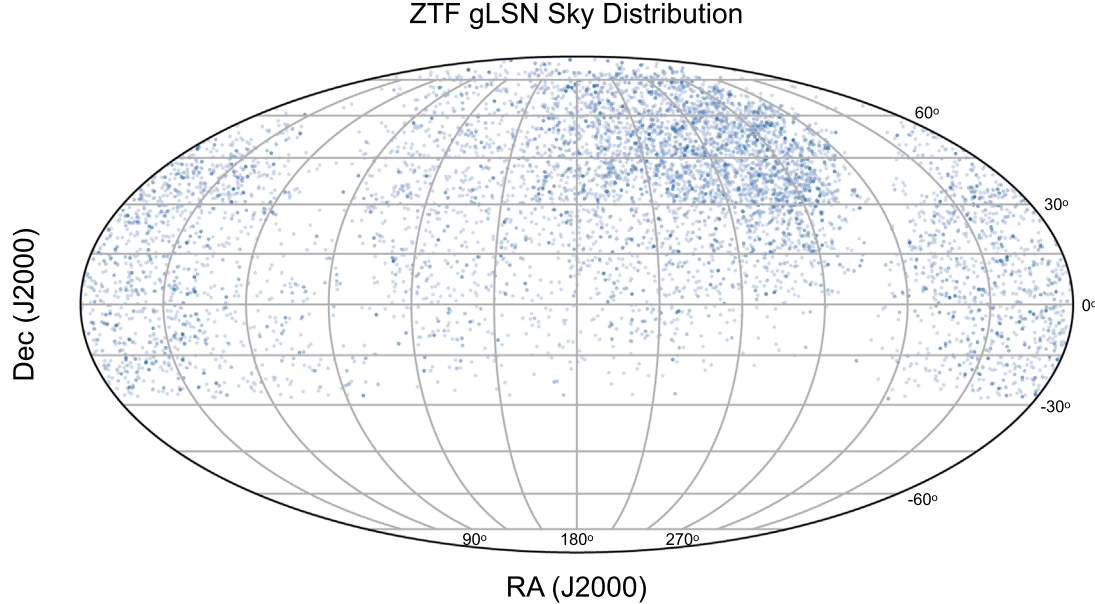


**Figure 8.** Model (i.e., noiseless) 6" × 6" composite *gri* images of 25 randomly chosen simulated gLSNe, their lens galaxies, and their lensed host galaxies, “detected” by LSST under the `minion_1016` observing strategy. Each image is “taken” exactly one night after the transient is detected as a gLSN candidate based on a light curve fit to the simulated LSST data (see Section 2.9). The FWHM of the seeing on the images is 0''.1, and the pixel scale is 0''.04, identical to that of the UVIS channel of WFC3. The systems in this mosaic are generally less compact and less magnified than those in Figure 7, reflecting the increased depth and red-sensitivity of LSST compared to ZTF.

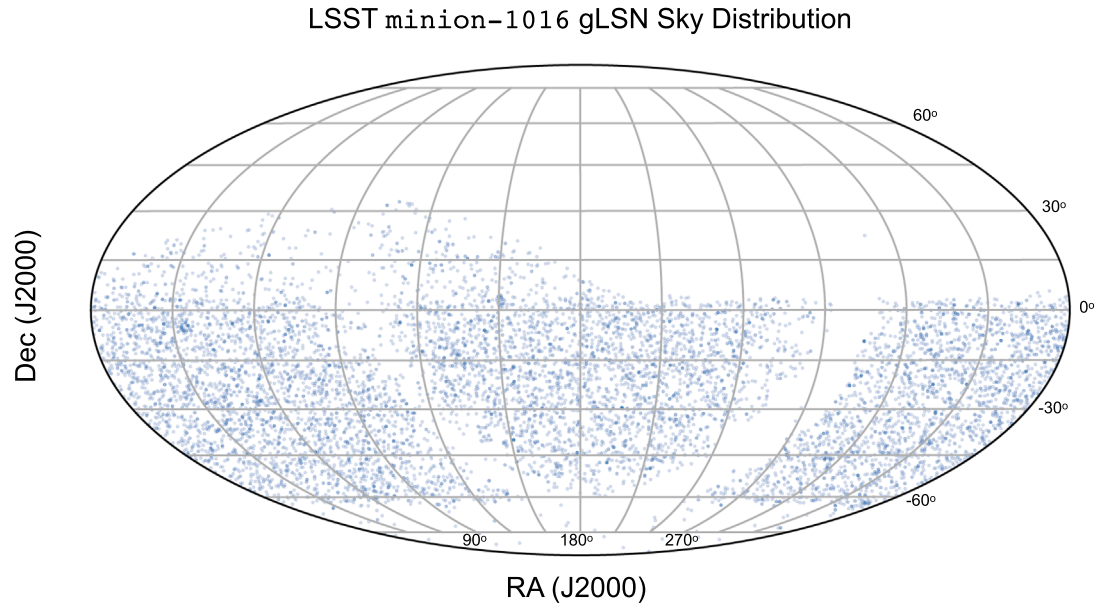
IIn. The Type IIn rates are given as lower limits because gLSNe IIn can be detected in both ZTF and LSST beyond  $z_s = 3$ , the maximum redshift in our simulations, but their rate at  $z_s > 3$  is highly speculative.

Color-composite images of randomly selected gLSNe, drawn in proportion to their weights, discovered by ZTF and LSST (minion\_1016) are shown in Figures 7 and 8, respectively. Figures 9 and 10 show the sky distributions of

detected gLSNe. Figures 11–25 summarize the results of our Monte Carlo simulations, presenting the distributions of several key observables and parameters of detected systems. Table 3 describes the subpanels in each figure, and red lines in histogram panels indicate medians. Figures 26–35 show multiband light curves of gLSNe from ZTF and LSST. In those figures, the solid lines reflect the true underlying light curves of each image, while the photometric data are realized



(a) Sky distribution of gLSNe (all types) detected by ZTF in the simulation (Mollweide projection, equatorial coordinates). The discovered gLSNe are concentrated in the high-cadence and *i*-band fields.



(b) Sky distribution of gLSNe (all types) detected by `minion-1016` in the simulation (Mollweide projection, equatorial coordinates). The discovered gLSNe are relatively uniformly distributed across the survey footprint, except for the Galactic plane, which has high extinction and yields almost no gLSNe, and the north ecliptic spur, which has high airmass and yields gLSNe at a reduced rate.

**Figure 9.** Sky distributions of gLSNe discovered in the simulations.

from the sum of the images. The ZTF photometry is unstacked, reflecting the survey’s high intranight cadence, whereas the LSST photometry is combined nightly into single point per filter for clarity. Figure 36 shows distributions of lensed host galaxy

apparent magnitudes and separations (relative to the lens centroid) in units of  $\theta_E$ . If the lens–host centroid distance is less than  $2\theta_E$ , there is a strong likelihood that the host galaxy is multiply imaged and can thus provide useful constraints on the lens model.

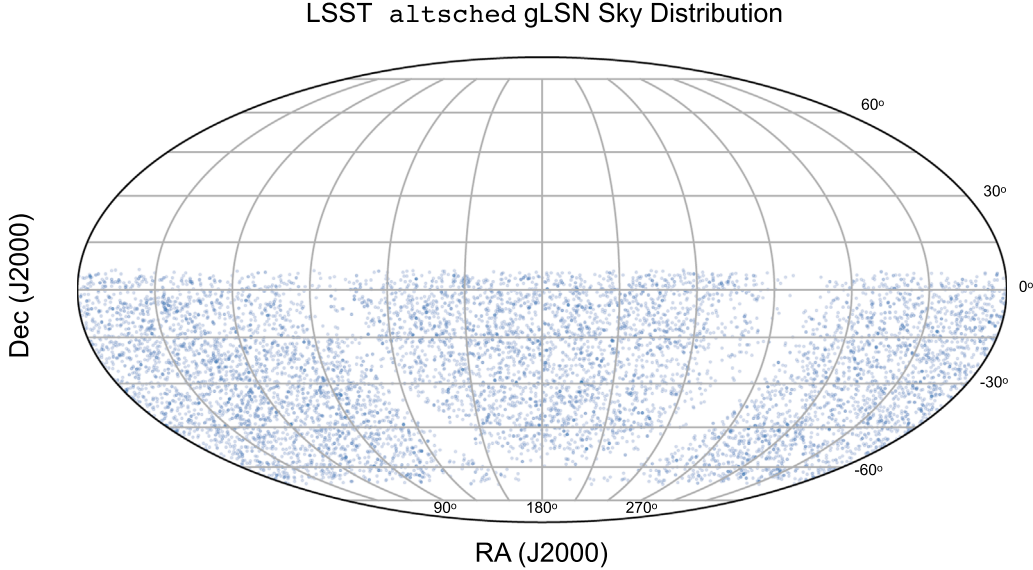


**Figure 10.** Sky distribution of gLSNe (all types) detected by `altsched` in the simulation (Mollweide projection, equatorial coordinates). The discovered gLSNe are uniformly distributed across the survey footprint, except for the Galactic plane, which has high extinction.

**Table 3**  
Description of the Subpanels in Figures 12–24

Subpanel	Description
a	Smallest angular separation, in arcseconds, between two images in the system (alternatively, the angular resolution required to completely resolve the system)
b	Largest time delay between two images in the system
c	Rest-frame phase of the blended light curve on the date of discovery relative to rest-frame <i>B</i> -band maximum
d	Peak observer-frame AB magnitude of the gLSN in <i>g</i> (ZTF) or <i>r</i> (LSST)
e	Peak observer-frame AB magnitude of the gLSN in <i>r</i> (ZTF) or <i>i</i> (LSST)
f	Peak observer-frame AB magnitude of the gLSN in <i>i</i> (ZTF) or <i>z</i> (LSST)
g	Source redshift
h	Lens redshift
i	Magnitude of the external shear
j	SIE velocity dispersion
k	Total lensing amplification of the gLSN images
l	Number of gLSN images in the system
m	Correlation between source and lens redshift, color coded by image multiplicity. Purple points correspond to double images, blue to quads, and redder colors to systems with more than four images.
n	Correlation between total magnification and image separation, color coded as (m)
o	Correlation between median image separation and median time delay, color coded as (m)

Figures 7–8, 11, 17, and 25 show that ZTF and LSST are sensitive to different populations of gLSNe. ZTF gLSNe have a median  $z_s = 0.9$ ,  $z_l = 0.35$ ,  $\mu_{\text{tot}} = 30$ ,  $\Delta t_{\text{max}} = 10$  days,  $\min \theta = 0.^{\circ}25$ , and  $N_{\text{img}} = 4$ . LSST gLSNe have a median  $z_s = 1.0$ ,  $z_l = 0.4$ ,  $\mu_{\text{tot}} \approx 6$ ,  $\Delta t_{\text{max}} = 25$  days,  $\min \theta = 0.^{\circ}6$ , and  $N_{\text{img}} = 2$ . Synthesizing this information, we find the ZTF gLSNe tend to be more compact, highly magnified, and have shorter time delays than their LSST counterparts. Additionally, ZTF gLSNe are more likely to be quads than gLSNe from LSST. The gLSN iPTF16geu discovered by ZTF’s predecessor iPTF was broadly consistent with this picture: it was a compact (med  $\theta \sim 0.^{\circ}3$ ) and highly magnified ( $\mu \sim 90$ ) quad with short time delays ( $\Delta t < 1$  day). The gLSNe from LSST will be better suited to time-delay cosmology. Their longer time delays and wider separations will enable more precise constraints on  $H_0$  and better models of the mass profile. However, they will be fainter and thus require larger telescopes and more observing

time for follow-up observations. Table 4 shows that just 10% of the gLSNe that ZTF will find will come from the public data alone. The proprietary data, notably the high-cadence data and the *i*-band survey, will be critical for discovering gLSNe.

## 4. Discussion

### 4.1. Comments on the LSST Observing Strategy

Broadly speaking, candidate observing strategies for LSST can be arranged on a spectrum in which area and season length are traded for sampling and depth. In this analysis, we have investigated strategies from both ends of this spectrum. `minion_1016` covers a large area with relatively poor light curve sampling, while `altsched` covers a smaller area with better sampling and greater depth. Table 2 shows that the nominal LSST observing strategy `minion_1016` discovers roughly the same number of gLSNe as the alternative strategy

**Table 4**

Fraction of gLSNe Discovered in the ZTF Simulation That Have *i*-band Data (Partnership), High-cadence Data (Partnership), and Exclusively MSIP (Public Survey) Data

SN Type	<i>i</i> [%]	High Cadence [%]	MSIP Only [%]
Type Ia	77.7	77.3	12.4
Type IIP	82.0	73.9	10.5
Type IIn	71.3	73.1	16.2
Type Ib/c	80.4	76.8	10.8
Type IIL	81.1	75.1	10.7
SN 1991bg-like	81.7	75.6	9.9
SN 1991T-like	77.3	75.5	13.0

altsched, and Figures 17 and 25 show that the greatest difference in the gLSNe discovered under the two strategies is the discovery phase (see panel (c) of both figures). altsched discovers gLSNe earlier than `minion_1016` due to its higher-quality light curves. A key result of this analysis is that for LSST, the improved light curve sampling and depth of surveys like altsched can compensate for the corresponding loss in area or season length by discovering more gLSNe per square degree. Moreover, the simulated altsched survey only used 85% of the total LSST observing time, so it is possible that the altsched yields presented here are too low by a factor of  $\sim 1.17$ . Because the gLSN yields of altsched are comparable to those of `minion_1016`, which has significantly more area ( $26,100 \text{ deg}^2$  compared to altsched's  $21,460 \text{ deg}^2$ ),<sup>12</sup> but the resulting light curves have significantly better sampling and are discovered earlier, we conclude that altsched is a superior strategy for finding gLSNe, enabling faster spectroscopic follow-up and more observations of gLSNe while they are in the achromatic phase (Goldstein et al. 2018).

#### 4.2. Host Galaxy Properties and Implications for Lens Modeling

Figure 36 suggests that in both ZTF and LSST, at least 90% of lensed host galaxy centroids will be within  $2\theta_E$  of their associated lens galaxy centroids, making it extremely likely that they will be multiply imaged. The median apparent magnitudes of the hosts from both surveys are roughly 22 in the redder filters, placing them well within reach of space-based imaging facilities such as *HST*, *James Webb Space Telescope*, and *WFIRST*, and larger ground-based facilities, especially those with adaptive optics systems. Combined with the fact that gLSNe fade away, enabling a more precise reconstruction of the lensed hosts compared to lensed AGNs, this suggests that host galaxy modeling will not be a limiting factor in gLSN time-delay cosmology.

#### 4.3. Triple Images and Other Exotic Configurations

Figures 7–8 and 11–25 show that ZTF and LSST will occasionally discover gLSNe with three or more than four lensed images. These exotic configurations are uncommon but legitimate predictions of our population model. Triple image

systems, such as row three, column five of Figure 8, are a consequence of ellipticity in the lens mass profile. When an SIE lens becomes sufficiently elliptical, part of its inner “diamond” caustic can extend beyond the outer “oval caustic” in a configuration known as a “naked cusp” (Collett & Cunningham 2016). If a source is located in the naked cusp, it will form three adjacent lensed images in a curve around the mass profile.

gLSNe with more than four images are even rarer than gLSNe lensed by naked cusps, but they may still be discovered occasionally with LSST (it is extremely unlikely that ZTF will find any). They are a consequence of a nonzero core radius in the SIE lens potential, which itself is a consequence of ellipticity. If a supernova is located sufficiently close to the core of an elliptical SIE, it is possible that more than four images will form; in our simulations, systems with as many as eight images formed. These systems are extremely magnified,  $\mu \sim 10^4\text{--}10^6$ , and have vanishingly small time delays and separations. For this reason, they may be straightforward to detect, but will provide almost no useful information for cosmology. They may, however, enable high signal-to-noise ratio spectroscopy of very high redshift supernovae, for which spectroscopy cannot currently be obtained. This would be useful for studying the evolution of the supernova population with redshift.

#### 4.4. Bimodal Lens Redshift Distribution for ZTF gLSNe Ia

As Figures 12(h) and 16(h) show, the lens redshift distributions for Type Ia and SN 1991T-like supernovae in ZTF are bimodal, with a first peak at  $z_l \approx 0.1$  and a second at  $z_l \approx 0.4$ . This is due to a selection effect introduced by the discovery strategy described in Section 2.9, which biases the survey against discovering SNe Ia with two images in lenses with  $z_l \gtrsim 0.15$ . In such systems, the flux amplification from lensing, which is usually on the order of a factor of a few, compensates for the reduction in flux caused by the fact that the supernova is at a higher redshift than the lens galaxy, making the overall flux of the transient compatible with an SN Ia hosted by the lens. Thus a dearth of gLSNe Ia with two images occurs for  $z_l \gtrsim 0.15$ , causing the bimodal distribution. Other types of gLSNe in ZTF do not have bimodal lens redshift distributions because of their core-collapse nature. The colors of core-collapse supernovae are so different from those of normal SNe Ia that they are still identified by the discovery when their overall fluxes are consistent with those of SNe Ia hosted by the lens galaxy.

#### 4.5. Prevalence of gLSNe IIn

Both ZTF and LSST will discover gLSNe IIn more frequently than any other gLSN subtype. SN Refsdal at  $z_s = 1.49$ , the first identified gLSN with resolved images, was a peculiar type of interacting supernova, similar to a Type IIn (Kelly et al. 2016). Relatively speaking, unlensed SNe IIn are uncommon, making up just 8%–12% of the observed core-collapse supernova rate (Li et al. 2011). However, SNe IIn are extremely bright (roughly 2 mag brighter than SNe IIP) and blue. Their colors are so different from those of SNe Ia that they are trivially identified by the discovery strategy detailed in Section 2.9. As their volumetric rate follows the star formation rate (see Figure 1), they are extremely common at high redshift (e.g., Petrushevska et al. 2016), just beyond the flux limit of most imaging surveys.

<sup>12</sup> The yields of gLSNe IIn appear to be higher in `minion_1016` than in altsched, but this is an artifact of the high redshifts needed to fully simulate the gLSN IIn population. The lower limits given have the ratio of the areas of the two surveys, indicating that both `minion_1016` and altsched are fully probing the population to  $z_s = 3$ . With an accurate model of the supernova rate at extremely high redshifts, it is likely that both `minion_1016` and altsched would converge to similar gLSN IIn yields.

Flux amplification from gravitational lensing will allow future synoptic imaging surveys to tap into this high-redshift population. This will enable unprecedented spectroscopic studies of the high-redshift core-collapse and interacting supernova populations. While in general the evolution of SNe IIn is slow, with the SED dominated by a blackbody continuum that slowly gets colder, several of these events show abrupt rises shortly after explosion, as well as periods in which the interaction increases or decreases abruptly. These may be suitable for time-delay measurements, but they will be the focus of future research. Because these gLSNe will be so numerous, increased focus should be placed on maximizing their scientific return.

#### 4.6. iPTF16geu: Remarkable Fluke or Evidence of Physics Not Captured by Current Lensing Models?

iPTF16geu (Goobar et al. 2017), the only gLSN Ia with resolved images discovered to date, is notable for its remarkably high magnification. Accounting for extinction, its four supernova images had a total magnification  $40 \lesssim \mu \lesssim 90$ , significantly larger than the predicted  $\mu \sim 25$  (More et al. 2017). Amplification by unresolved lens galaxy stars (microlensing) was proposed as an explanation for this anomaly (More et al. 2017). In a subsequent investigation, Yahalomi et al. (2017) used ray-tracing simulations to show that microlensing alone could not account for the large observed flux anomalies. This may indicate that the anomaly is due to millilensing, but a systematic study of millilensing induced by lens-galaxy substructures on gLSNe has yet to be performed.

Thus the origin of the large magnification of iPTF16geu remains a mystery, but the simulations presented in this paper can help place this discrepancy in context. iPTF, the survey that found iPTF16geu, used the same telescope as ZTF (the P48) to observe the same region of sky to roughly the same depth, but at a lower cadence. Thus the ZTF results presented here should

be quite similar to those for iPTF. Figure 37 shows the joint distribution of  $z_s$  and  $\mu_{\text{tot}}$  for gLSNe Ia discovered in ZTF, showing that iPTF16geu is significantly more magnified than expected for its redshift ( $>5\sigma$ ). Was iPTF16geu a remarkable fluke, or is there fundamental physics at play that our models for lensing do not capture? Searches for new strongly lensed SNe with ZTF will likely resolve this intriguing question.

## 5. Conclusion

In this article, we have presented detailed simulations of the gLSN population and made predictions of the properties and rates of gLSNe that forthcoming synoptic time-domain imaging surveys will find. ZTF should discover roughly 20 gLSNe over the course of a three-year survey, and LSST should find roughly 3500 over its 10 yr lifetime. Most host galaxies will be multiply imaged, enabling detailed lens modeling if sufficiently deep high-resolution imaging is obtained. ZTF and LSST are sensitive to different gLSN populations. ZTF is most sensitive to compact, highly magnified quads with short time delays, whereas LSST is more sensitive to fainter doubles, which in general are less magnified and have longer delays. This will give LSST an advantage for time-delay cosmology if it can obtain the follow-up resources needed to extract spectroscopy and time delays from these transients. Our inclusion of dust decreases the expected gLSN Ia rate over the predictions of Goldstein et al. (2018), which did not include dust, by a factor of  $\sim 2$ , but the predictions remain largely consistent with those of Goldstein & Nugent (2017). This study has found that gLSNe IIn will be the most frequently discovered by both ZTF and LSST. With respect to LSST observing strategy, we find that strategies that produce dense light curves at the expense of a larger survey area can yield comparable numbers of gLSNe, but the better-sampled surveys discover these gLSNe earlier and produce higher-quality light curves.

## ZTF: Multiply-Imaged SNe (All)

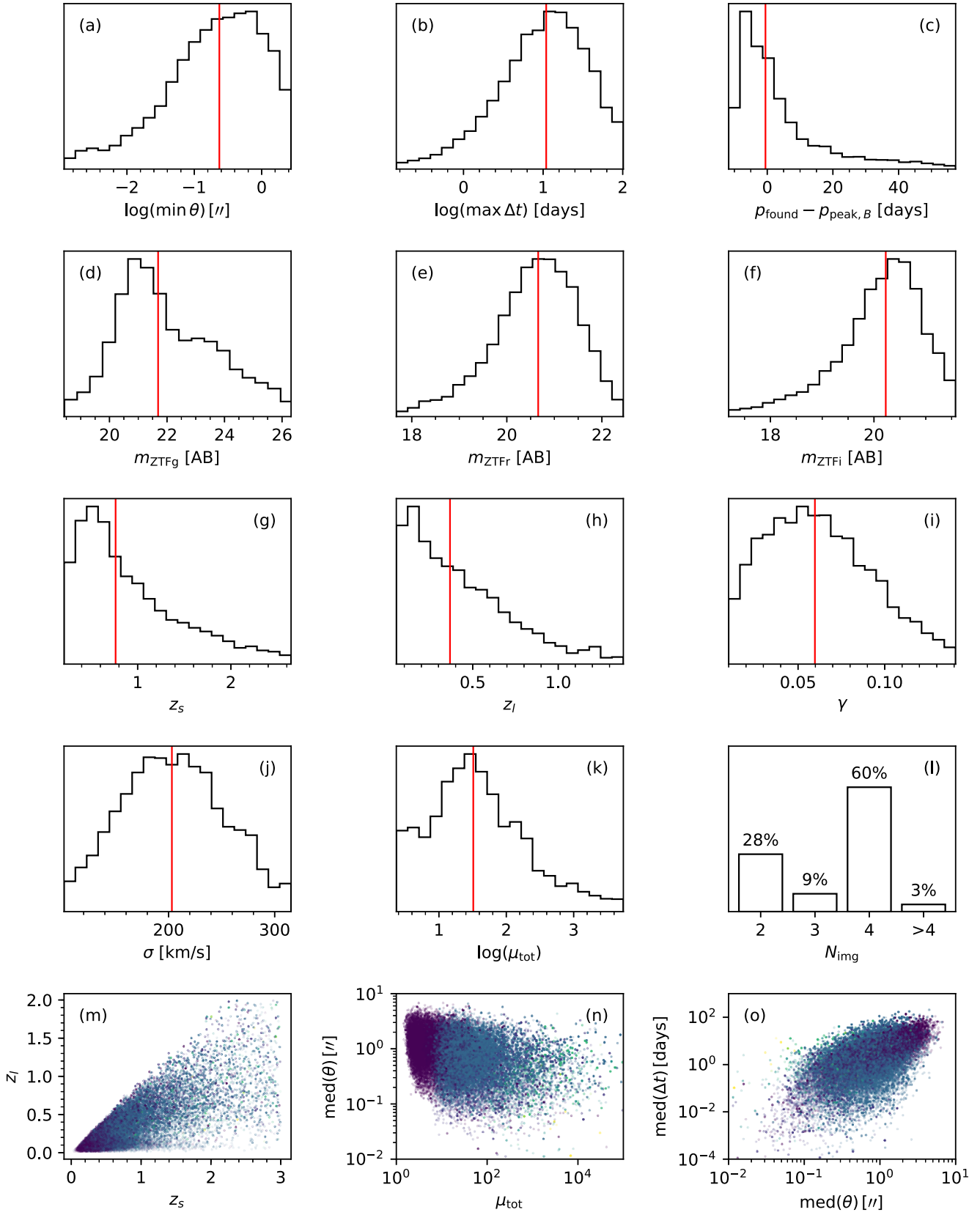


Figure 11. Monte Carlo results for ZTF supernovae (all types). See Table 3 for a description of each subplot.

## ZTF: Multiply-Imaged SNe Ia

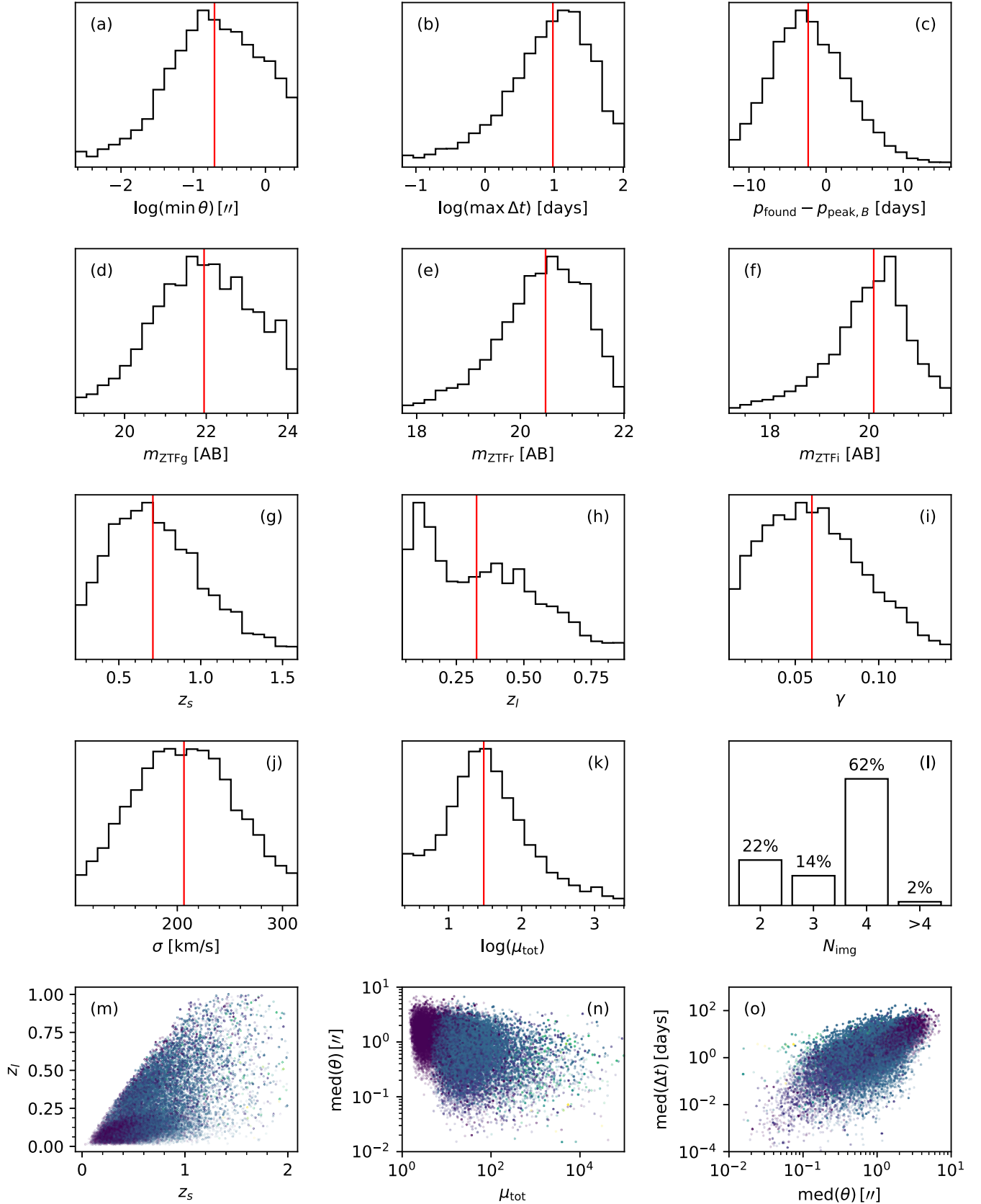


Figure 12. Monte Carlo results for ZTF SNe Ia. See Table 3 for a description of each subplot.

## ZTF: Multiply-Imaged SNe Ib/c

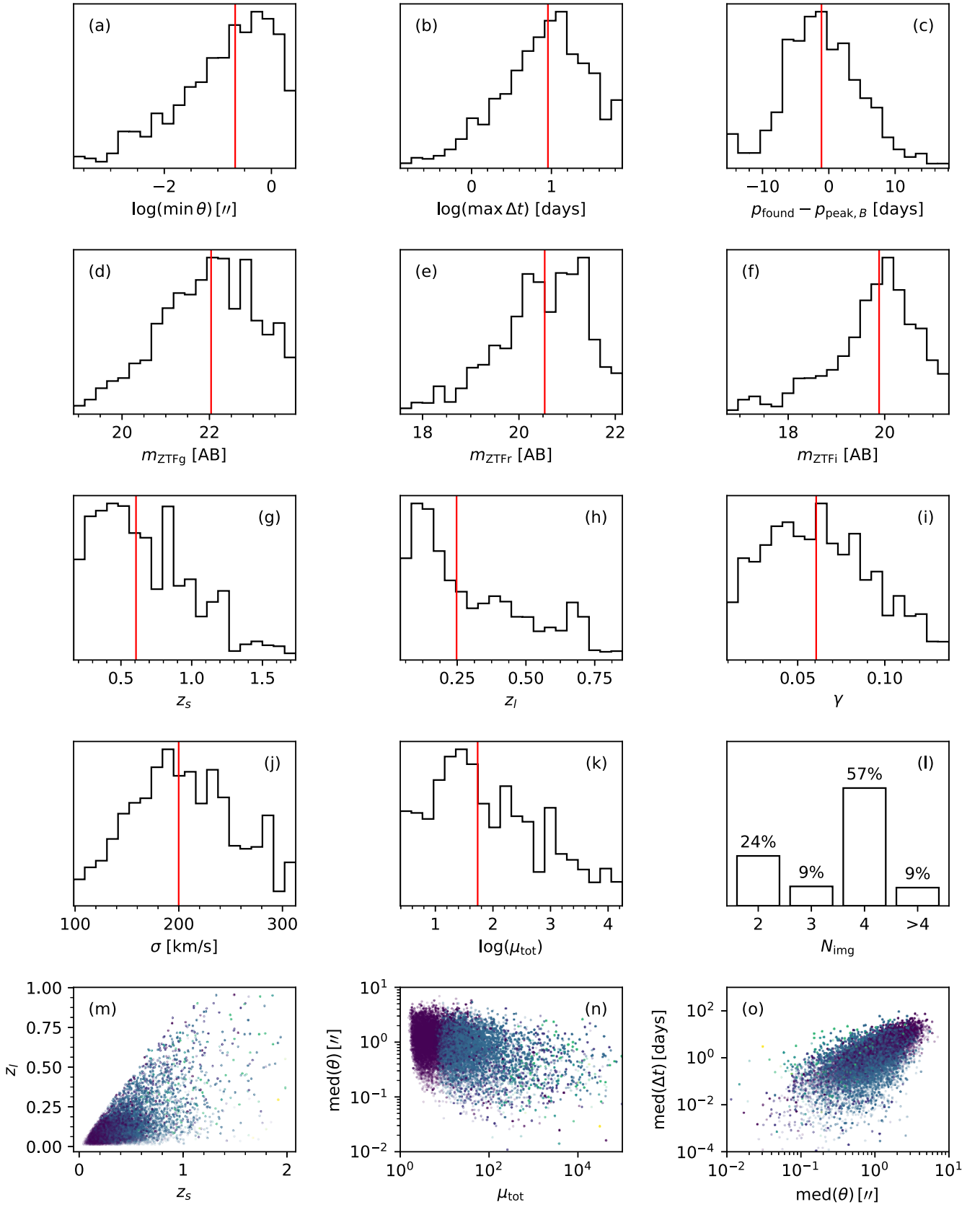


Figure 13. Monte Carlo results for ZTF SNe Ib/c. See Table 3 for a description of each subpanel.

## ZTF: Multiply-Imaged SNe IIn

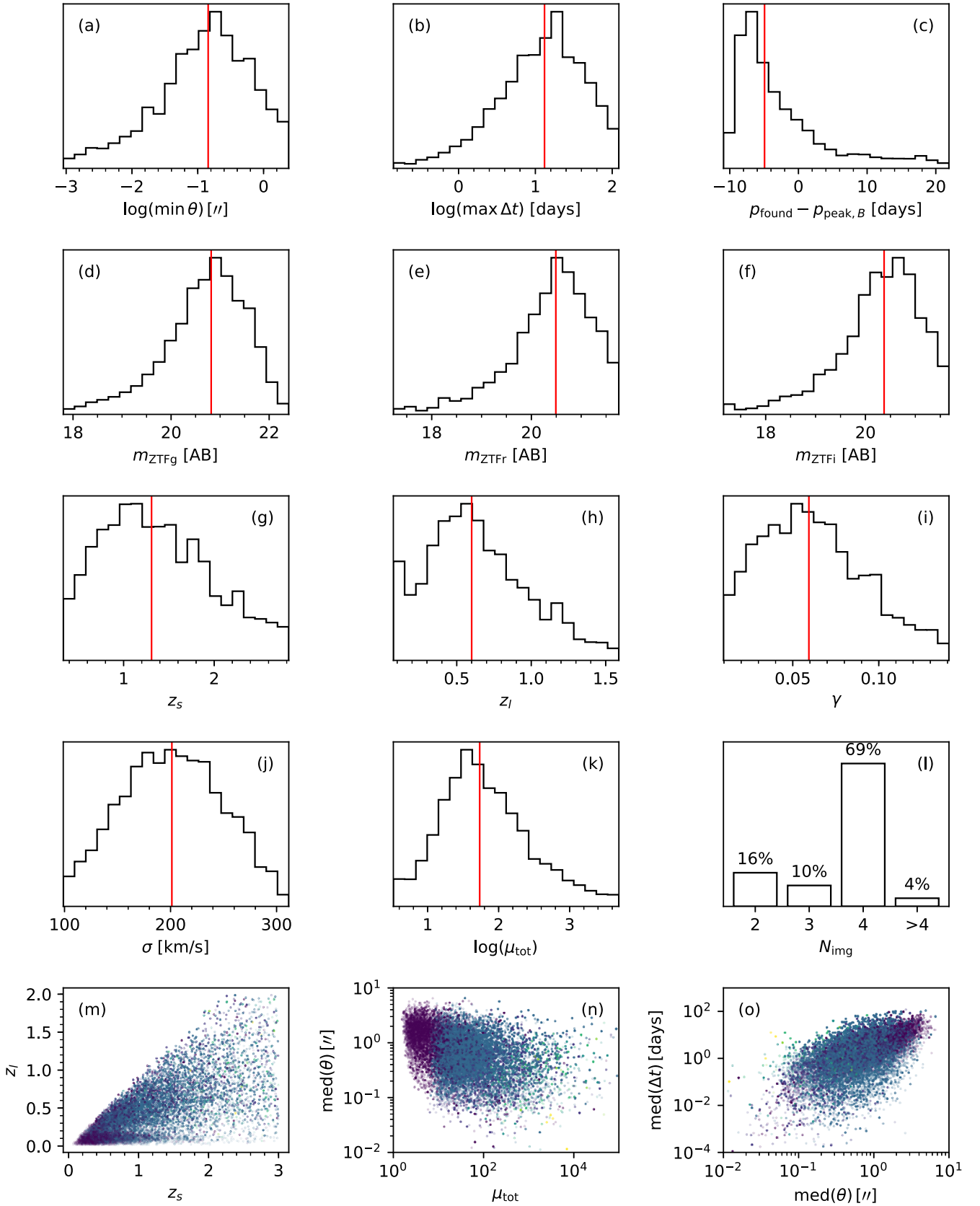


Figure 14. Monte Carlo results for ZTF SNe IIn. See Table 3 for a description of each subpanel.

## ZTF: Multiply-Imaged SNe IIP

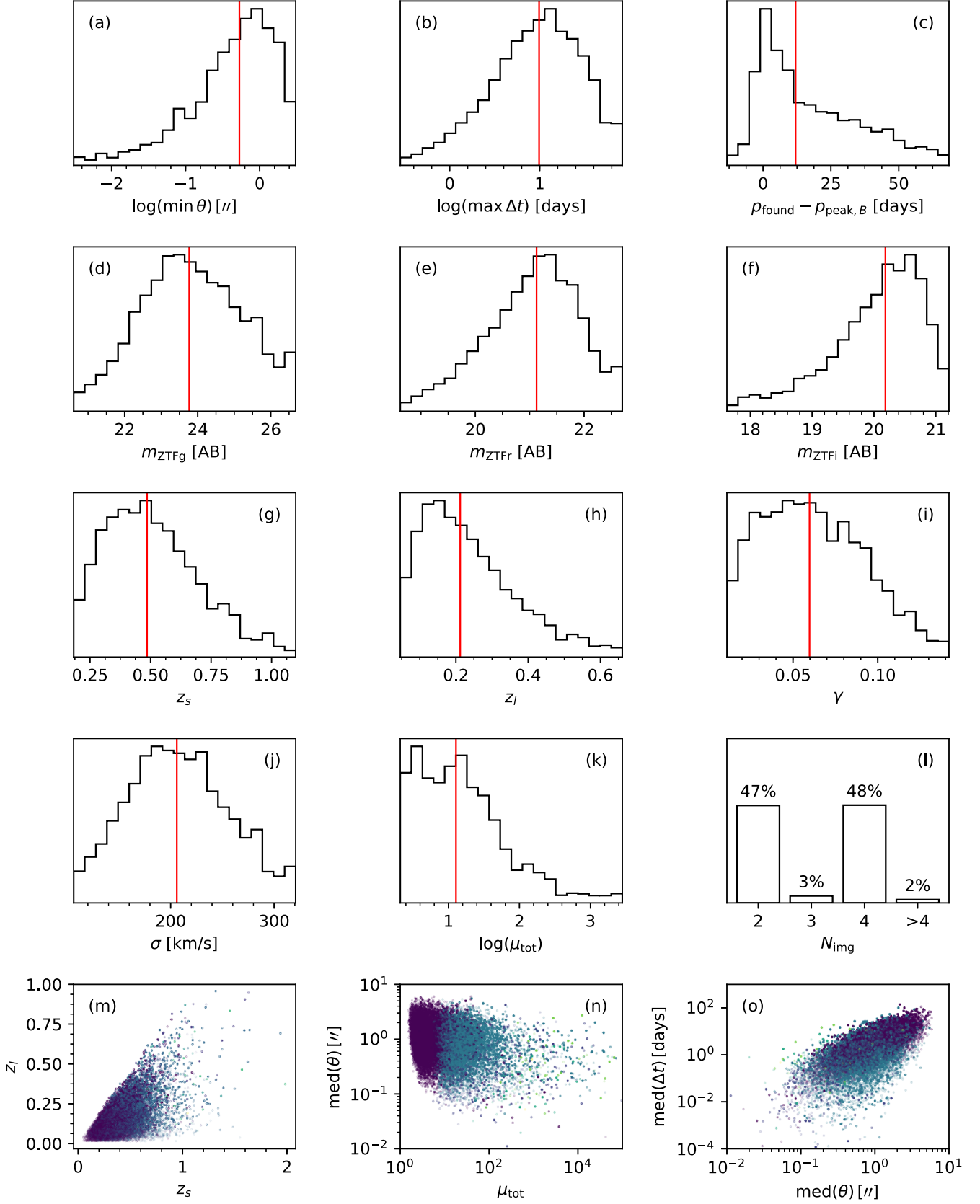


Figure 15. Monte Carlo results for ZTF SNe IIP. See Table 3 for a description of each subplot.

## ZTF: Multiply-Imaged 1991T-like SNe

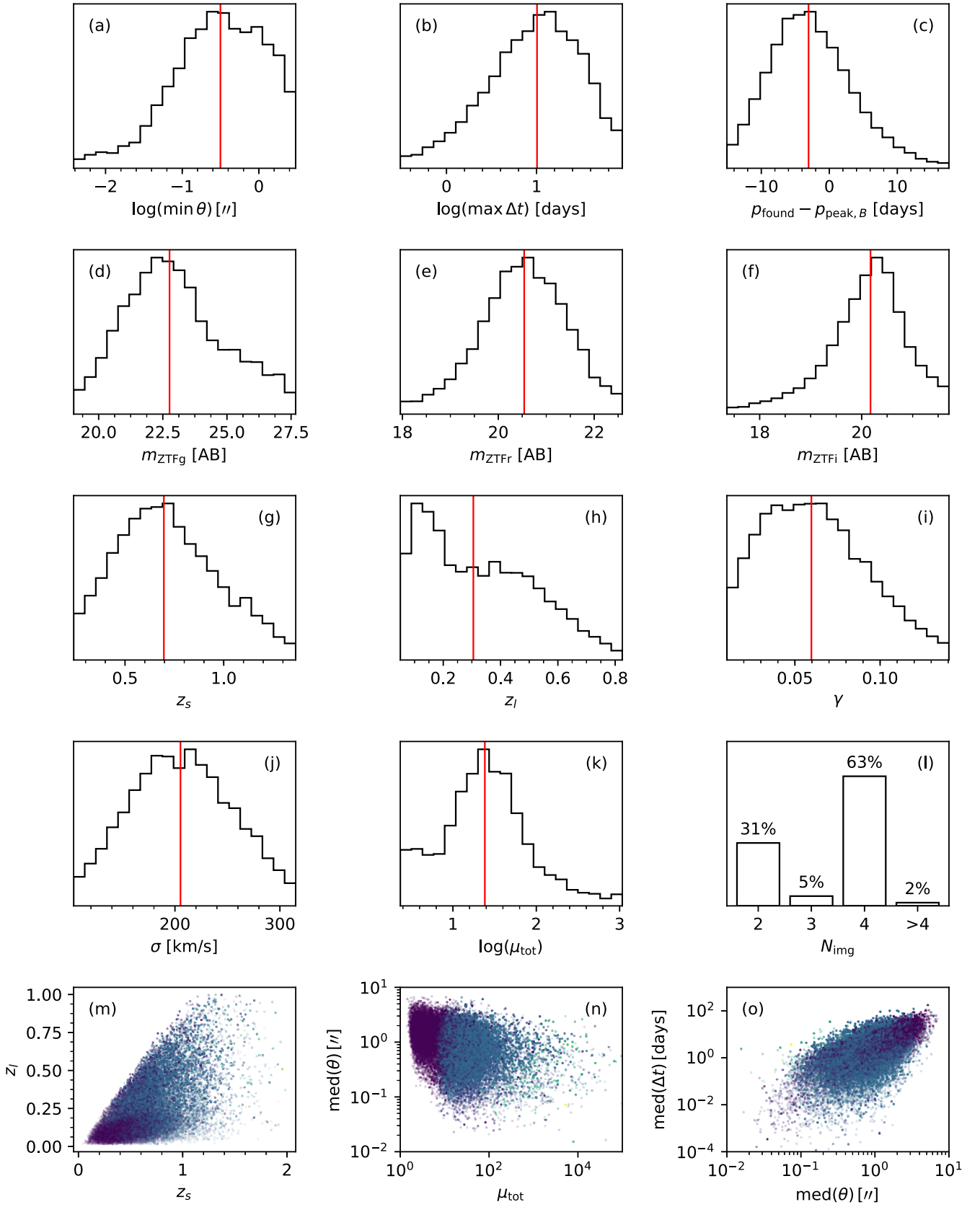
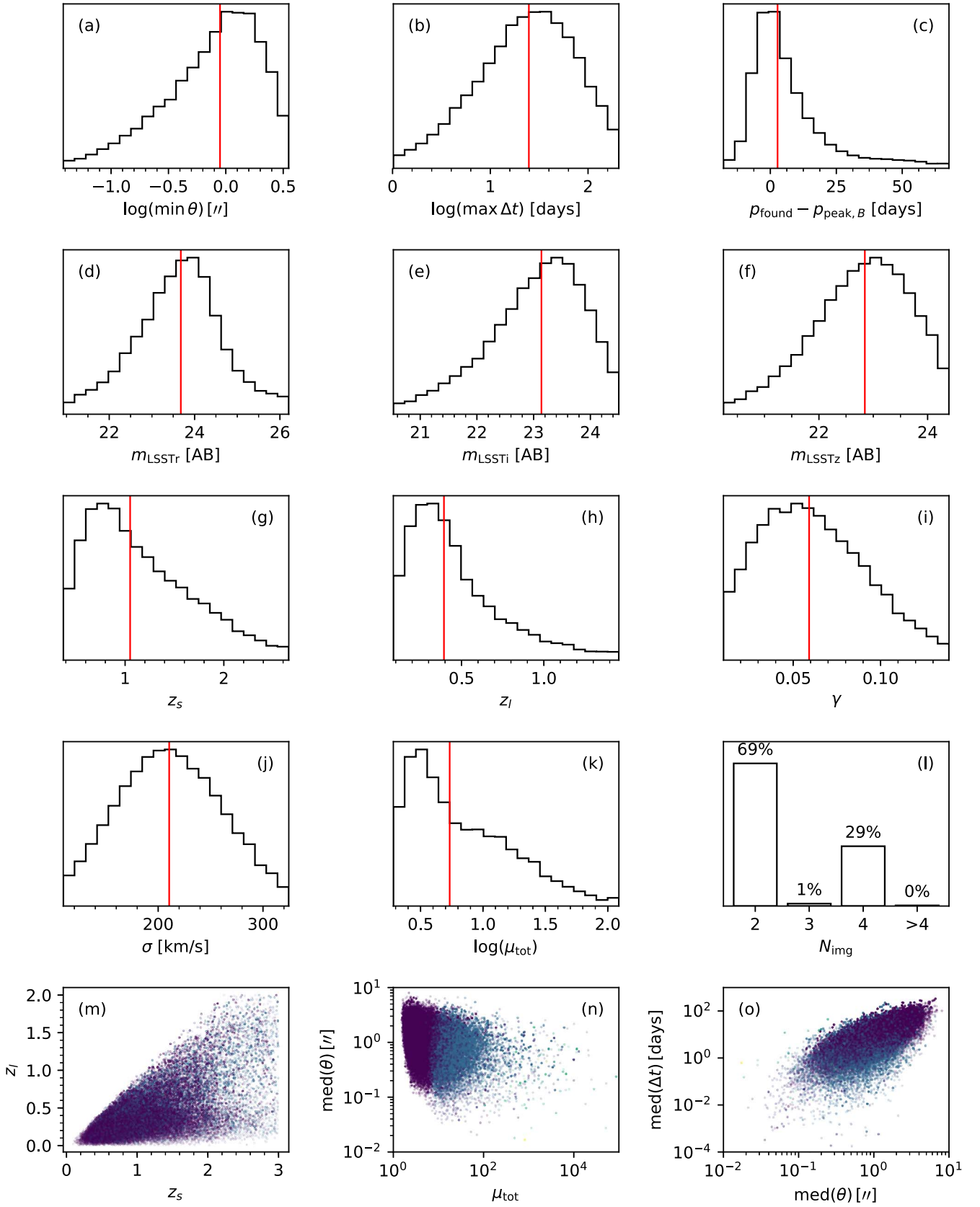


Figure 16. Monte Carlo results for ZTF SN 1991T-like supernovae. See Table 3 for a description of each subpanel.

## LSST (Minion-1016): Multiply-Imaged SNe (All)



**Figure 17.** Monte Carlo results for LSST (minion\_1016) supernovae (all subtypes). See Table 3 for a description of each subpanel.

## LSST (Minion-1016): Multiply-Imaged SNe Ia

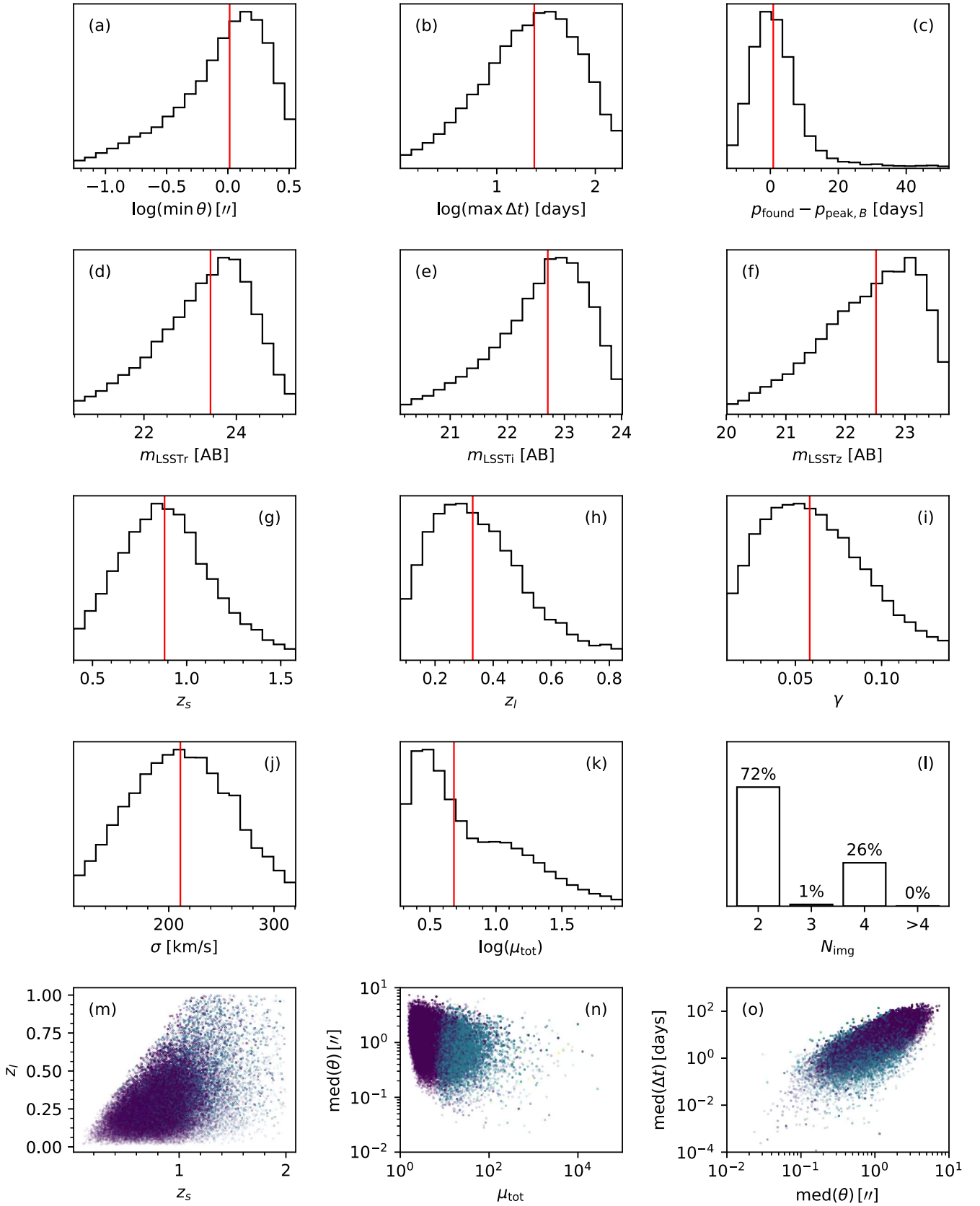


Figure 18. Monte Carlo results for LSST (minion\_1016) SNe Ia. See Table 3 for a description of each subplot.

## LSST (Minion-1016): Multiply-Imaged SNe Ib/c

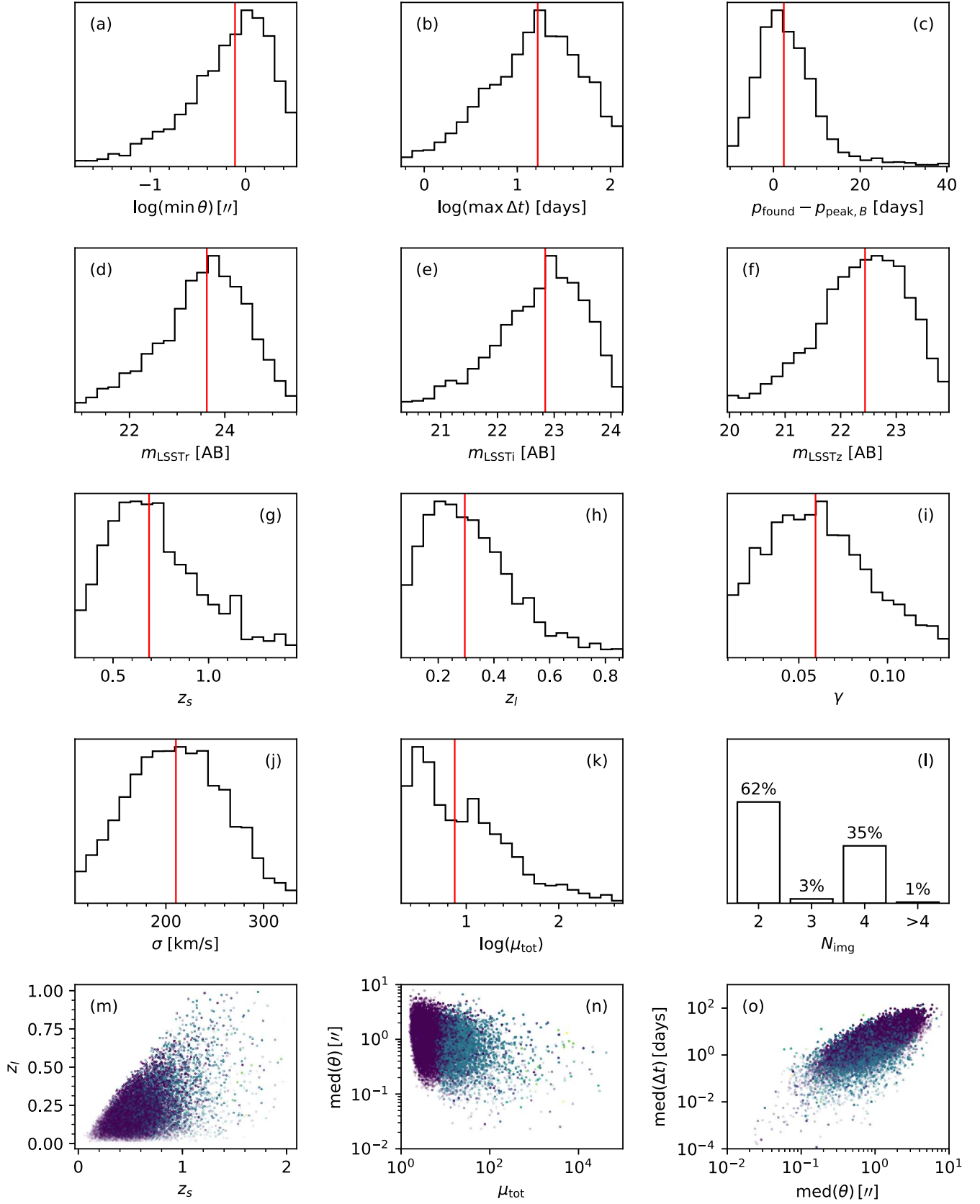


Figure 19. Monte Carlo results for LSST (minion\_1016) SNe Ib/c. See Table 3 for a description of each subpanel.

## LSST (Minion-1016): Multiply-Imaged SNe III

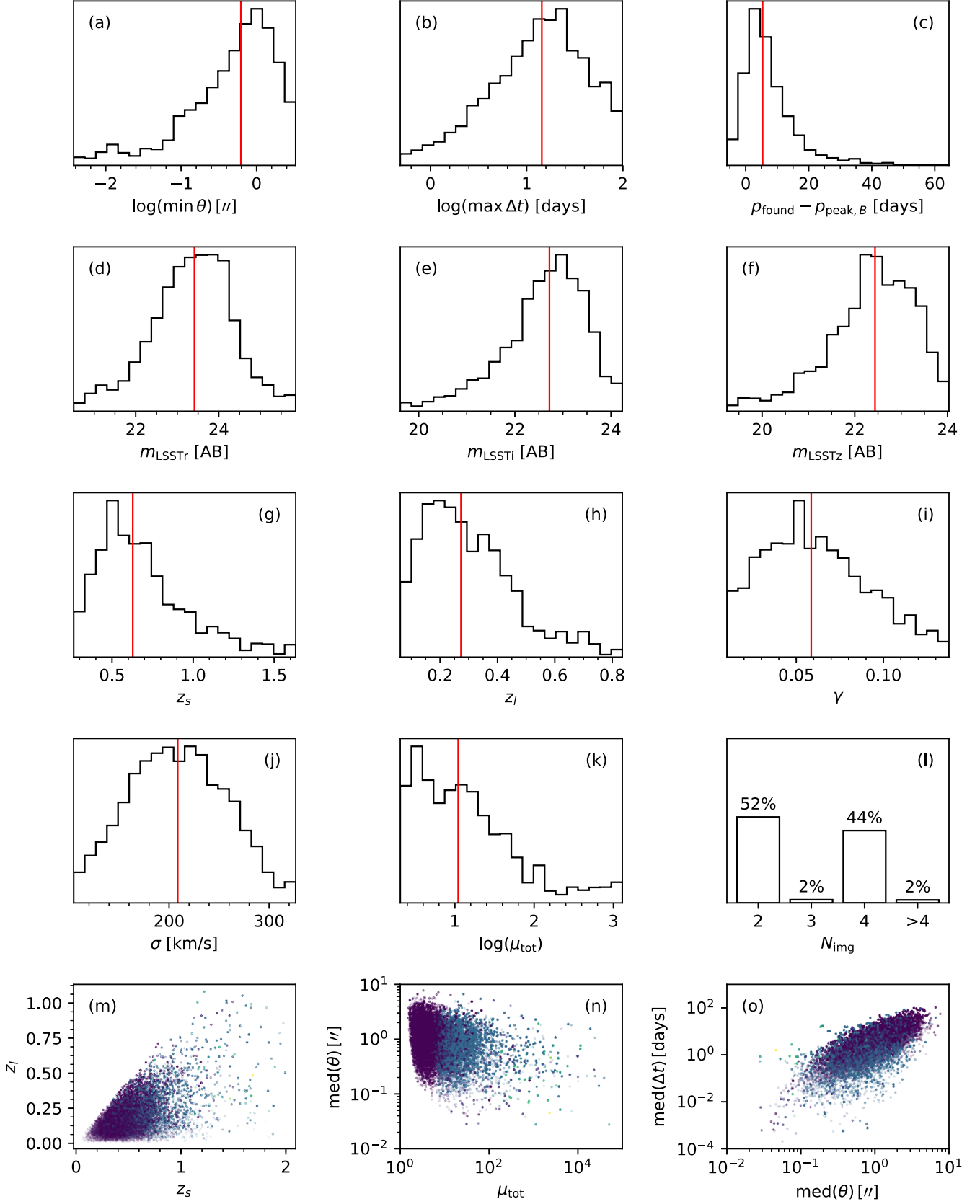
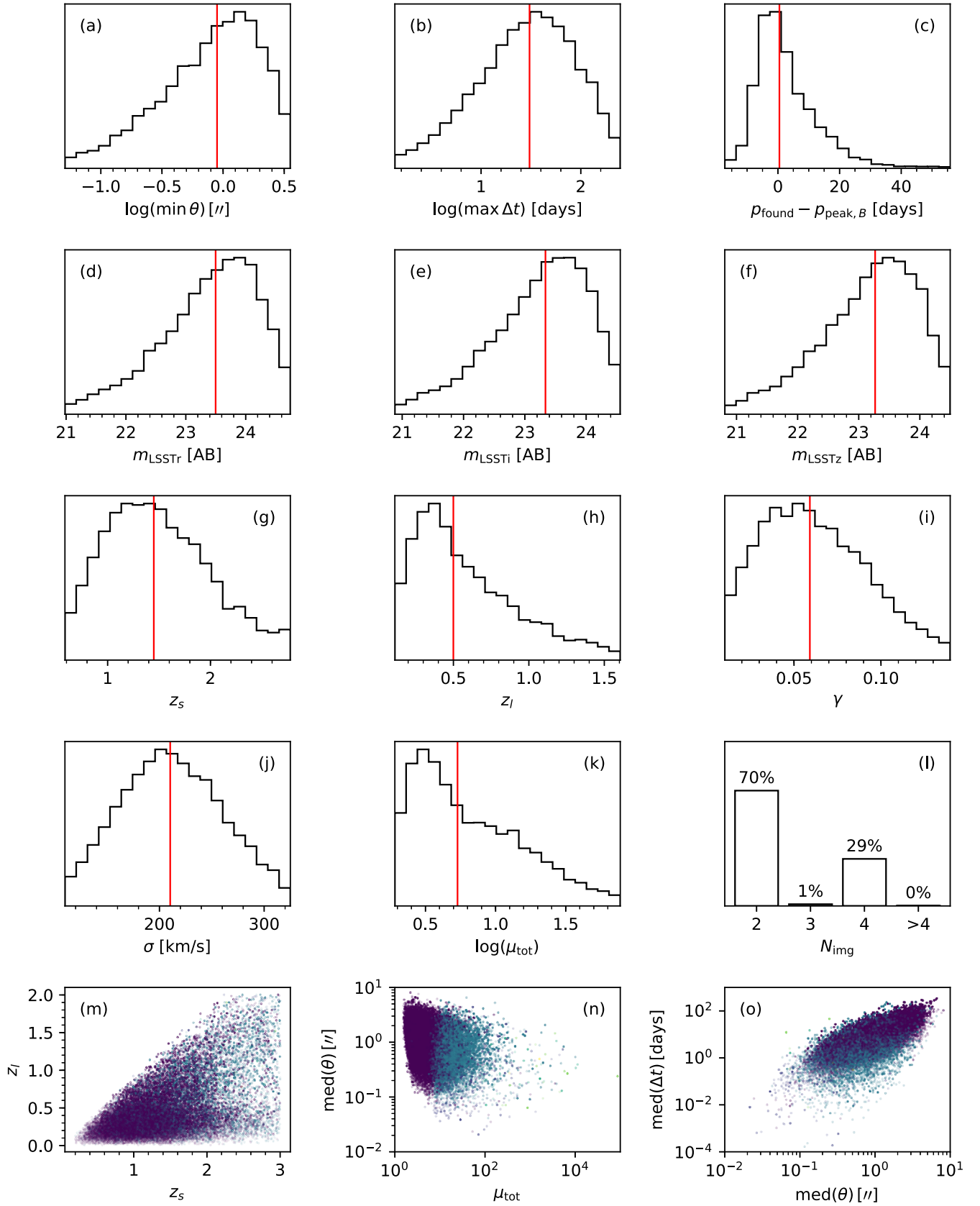
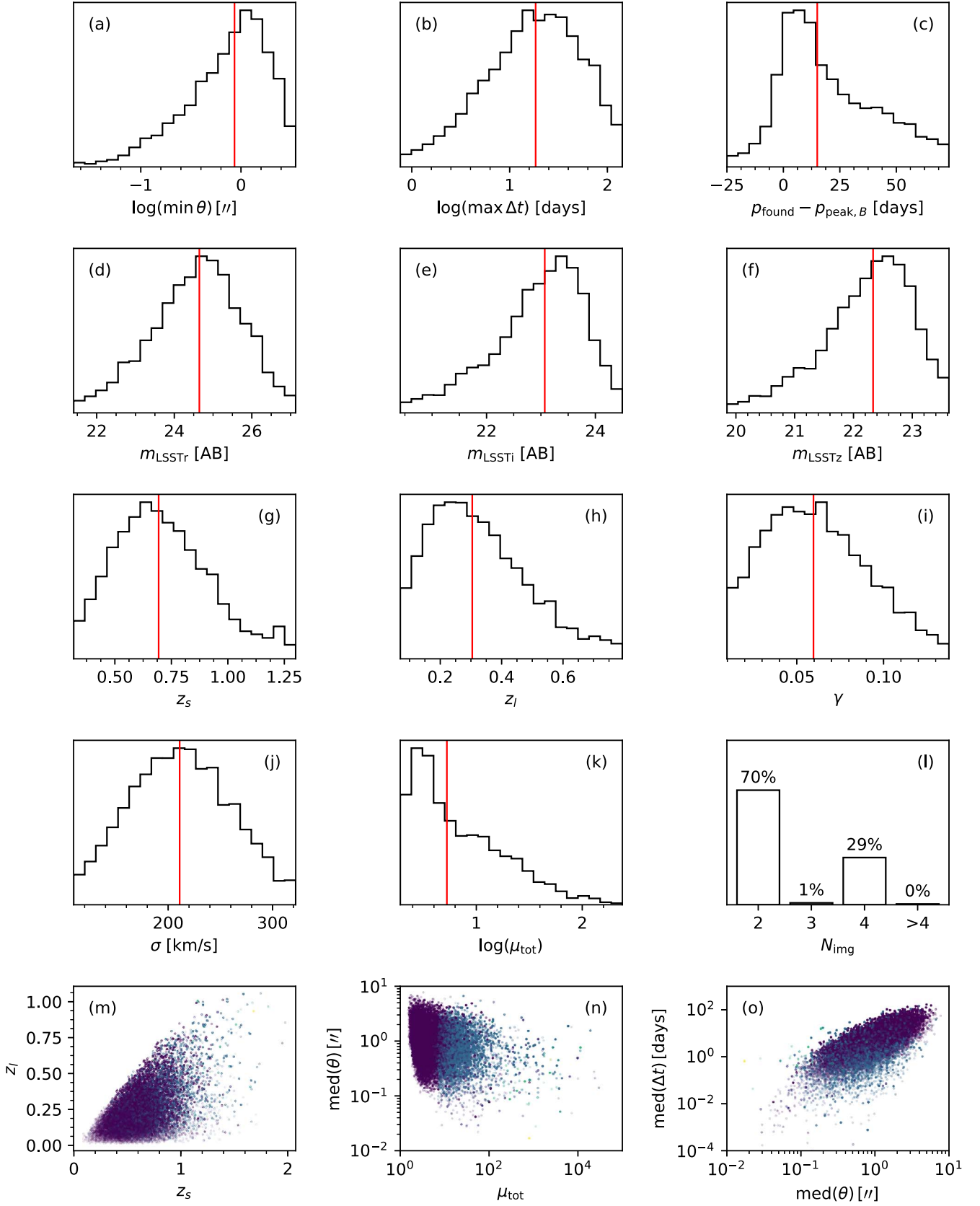


Figure 20. Monte Carlo results for LSST (minion\_1016) SNe III. See Table 3 for a description of each subpanel.

## LSST (Minion-1016): Multiply-Imaged SNe IIn

**Figure 21.** Monte Carlo results for LSST (minion\_1016) SNe IIn. See Table 3 for a description of each subpanel.

## LSST (Minion-1016): Multiply-Imaged SNe IIP

**Figure 22.** Monte Carlo results for LSST (minion\_1016) SNe IIP. See Table 3 for a description of each subpanel.

## LSST (Minion-1016): Multiply-Imaged 1991bg-like SNe

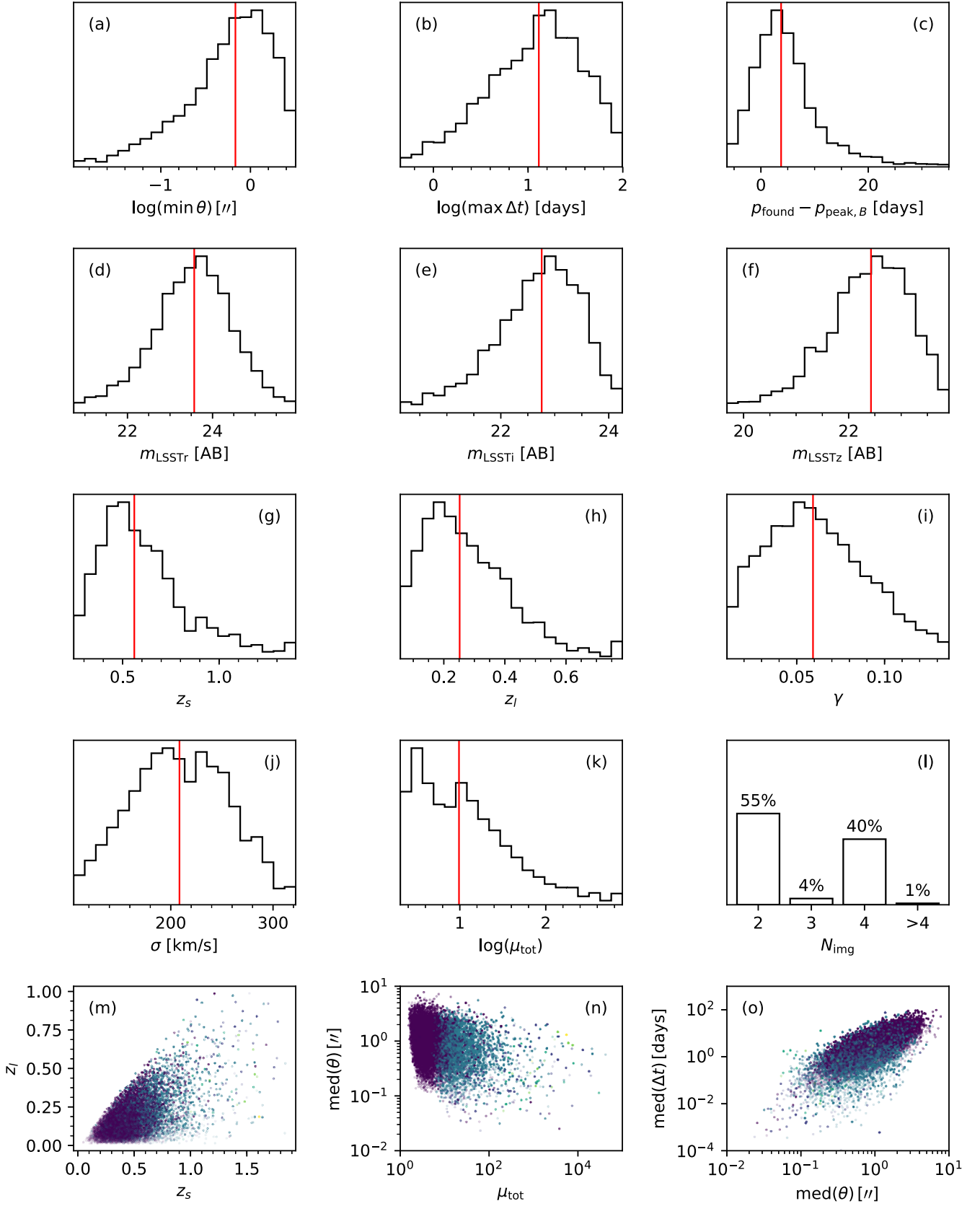


Figure 23. Monte Carlo results for LSST (minion\_1016) SN 1991bg-like supernovae. See Table 3 for a description of each subplot.

## LSST (Minion-1016): Multiply-Imaged 1991T-like SNe

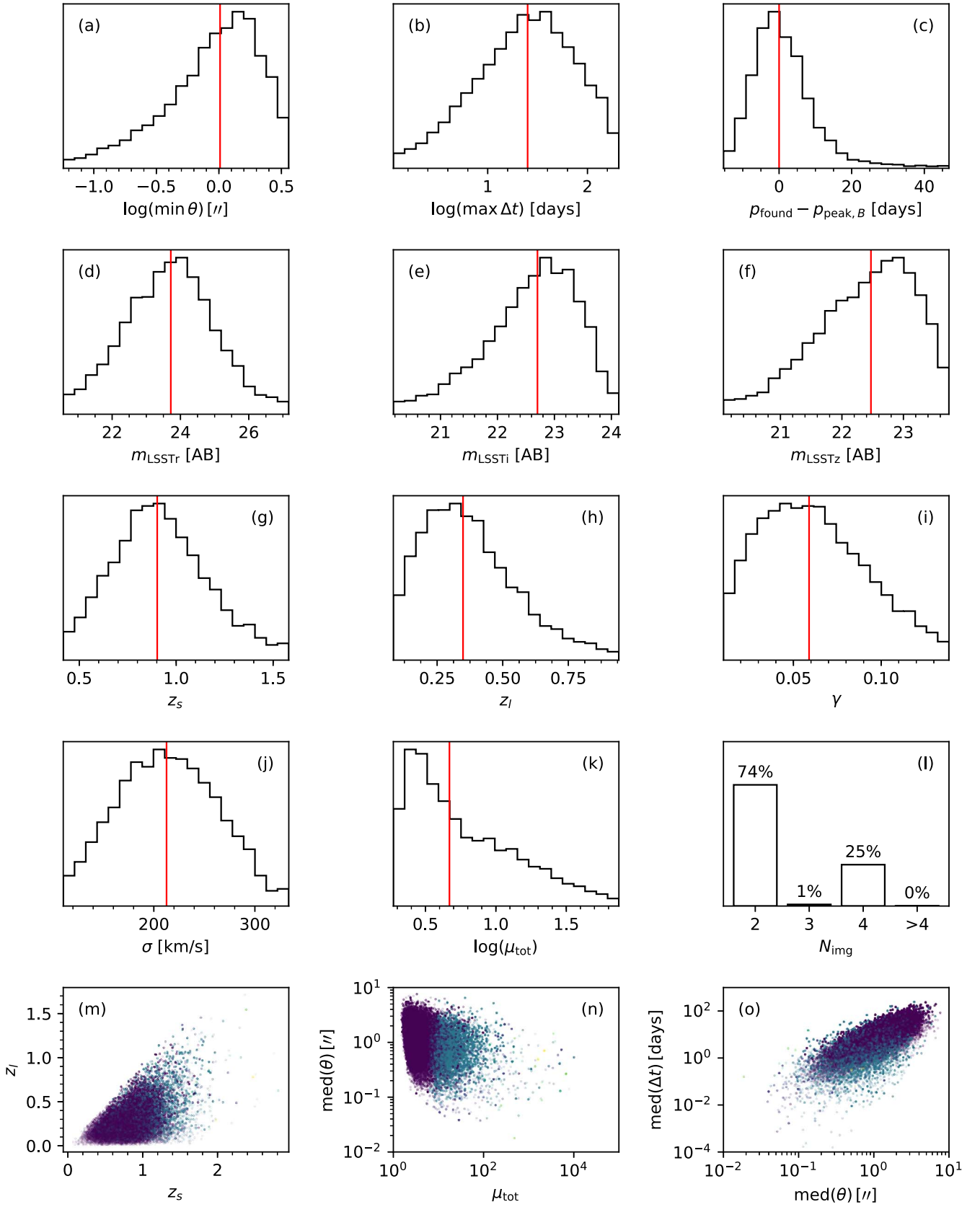
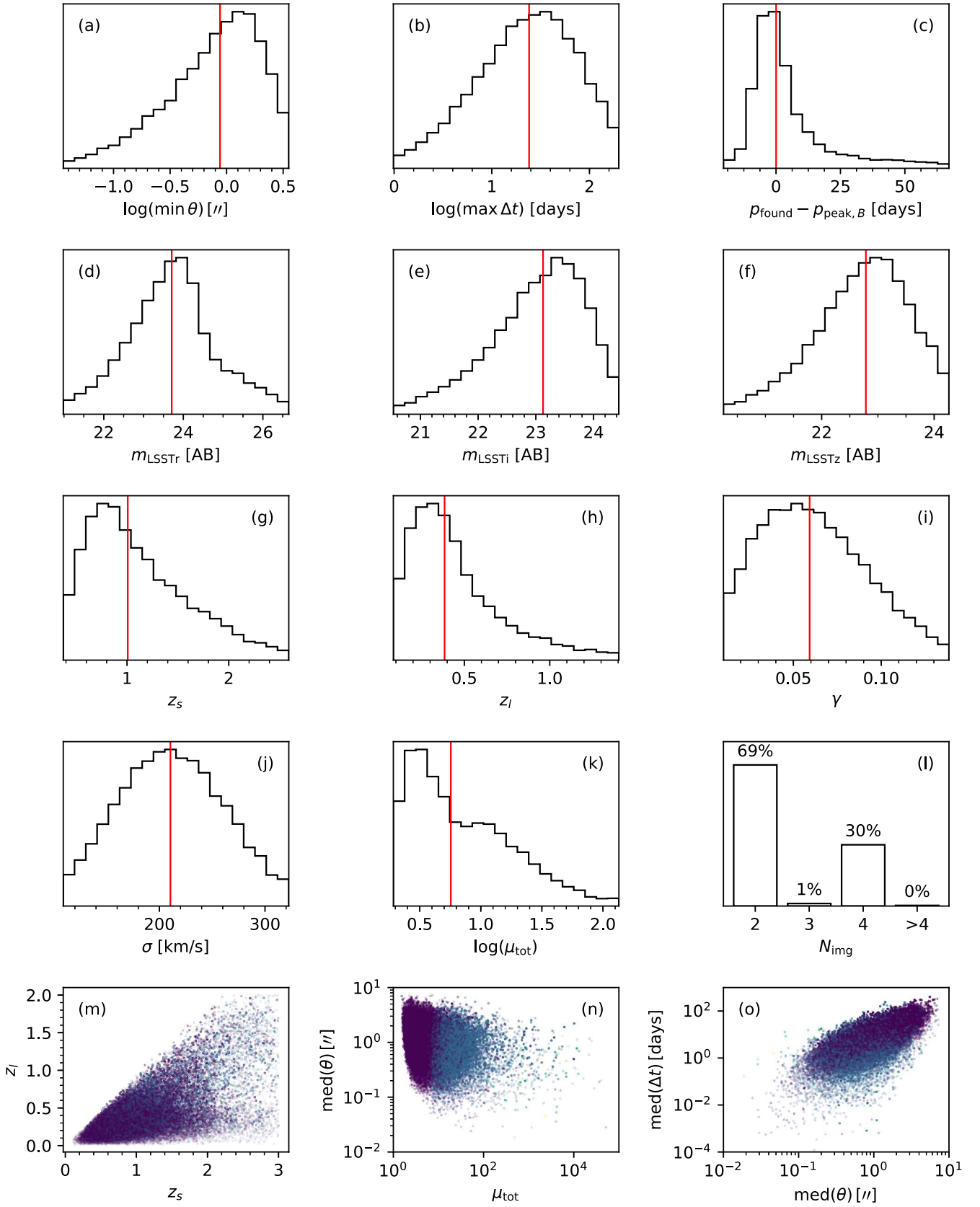
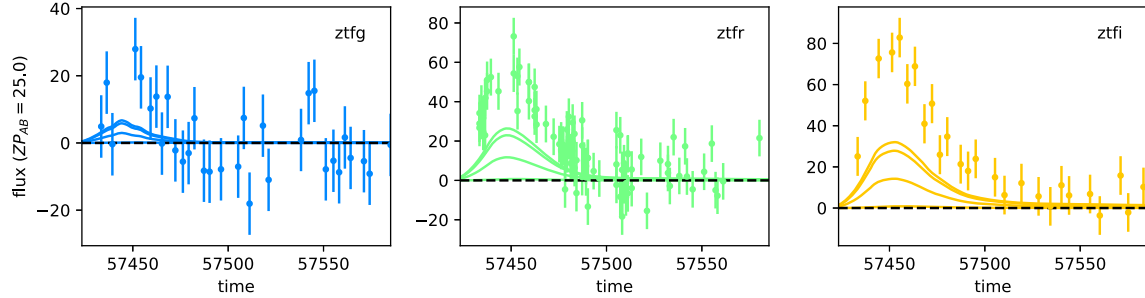


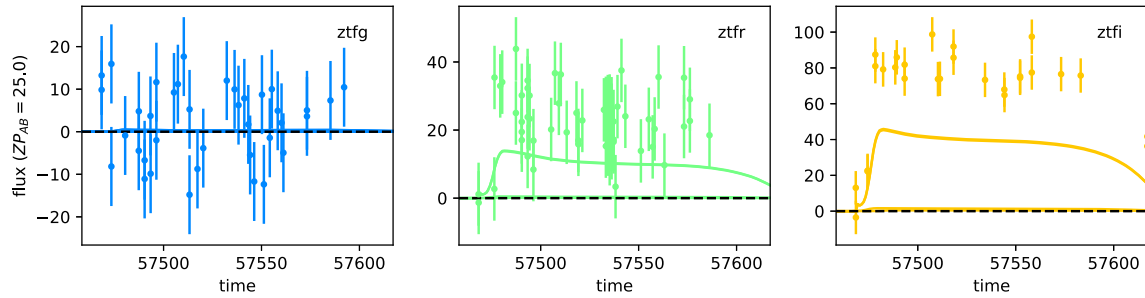
Figure 24. Monte Carlo results for LSST (minion\_1016) SN 1991T-like supernovae. See Table 3 for a description of each subplot.

## LSST (Altsched): Multiply-Imaged SNe (All)

**Figure 25.** Monte Carlo results for LSST (altsched) supernovae (all types). See Table 3 for a description of each subpanel.

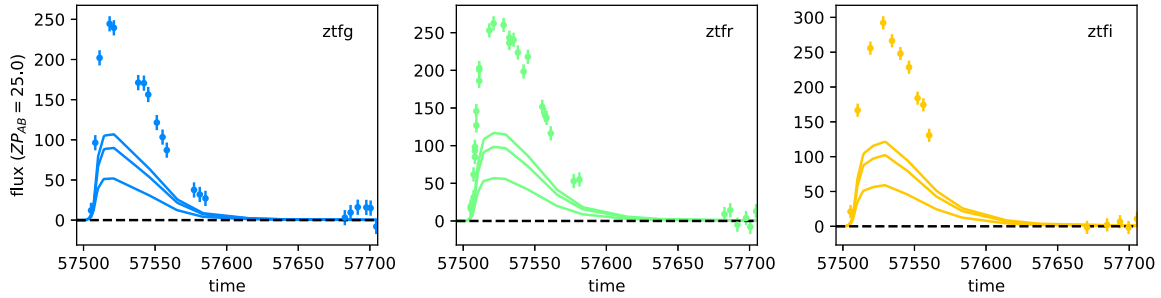


(a) Light curves of a quadruply-imaged gLSN Ia with  $z_s = 0.74$ ,  $z_l = 0.38$ . The images have time delays (relative to the earliest image) of 0.08, 0.10, and 4.46 days, and lensing amplifications of 8.9, 4.6, 10.3, and 0.3.

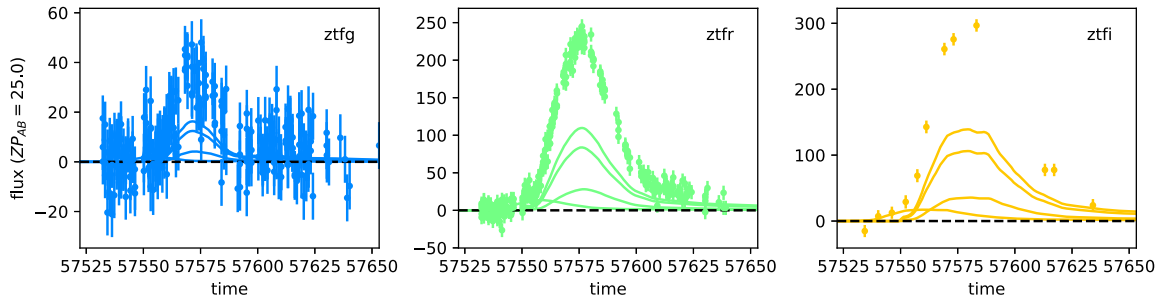


(b) Light curves of a quadruply-imaged gLSN IIP with  $z_s = 0.69$ ,  $z_l = 0.42$ . The images have time delays (relative to the earliest image) of 7.6, 2.1, and 2.1 days, and lensing amplifications of 2.8, 0.8, 76.6, and 77.7.

**Figure 26.** Simulated ZTF light curves of gLSNe. The solid lines show the model light curves of the individual images. The photometric data are realized from the sum of the model light curves.



(a) Light curves of a triply-imaged gLSN IIIn with  $z_s = 0.38$ ,  $z_l = 0.15$ . The images have time delays (relative to the earliest image) of 0.34 and 0.30 days, and lensing amplifications of 4.2, 8.7, and 7.3.



(b) Light curves of a quadruply-imaged gLSN Ib/c with  $z_s = 0.62$ ,  $z_l = 0.40$ . The images have time delays (relative to the earliest image) of 18.74, 17.75, and 17.72 days, and lensing amplifications of 6.1, 3.0, 18.1, and 23.6.

**Figure 27.** Simulated ZTF light curves of gLSNe. The solid lines show the model light curves of the individual images. The photometric data are realized from the sum of the model light curves.

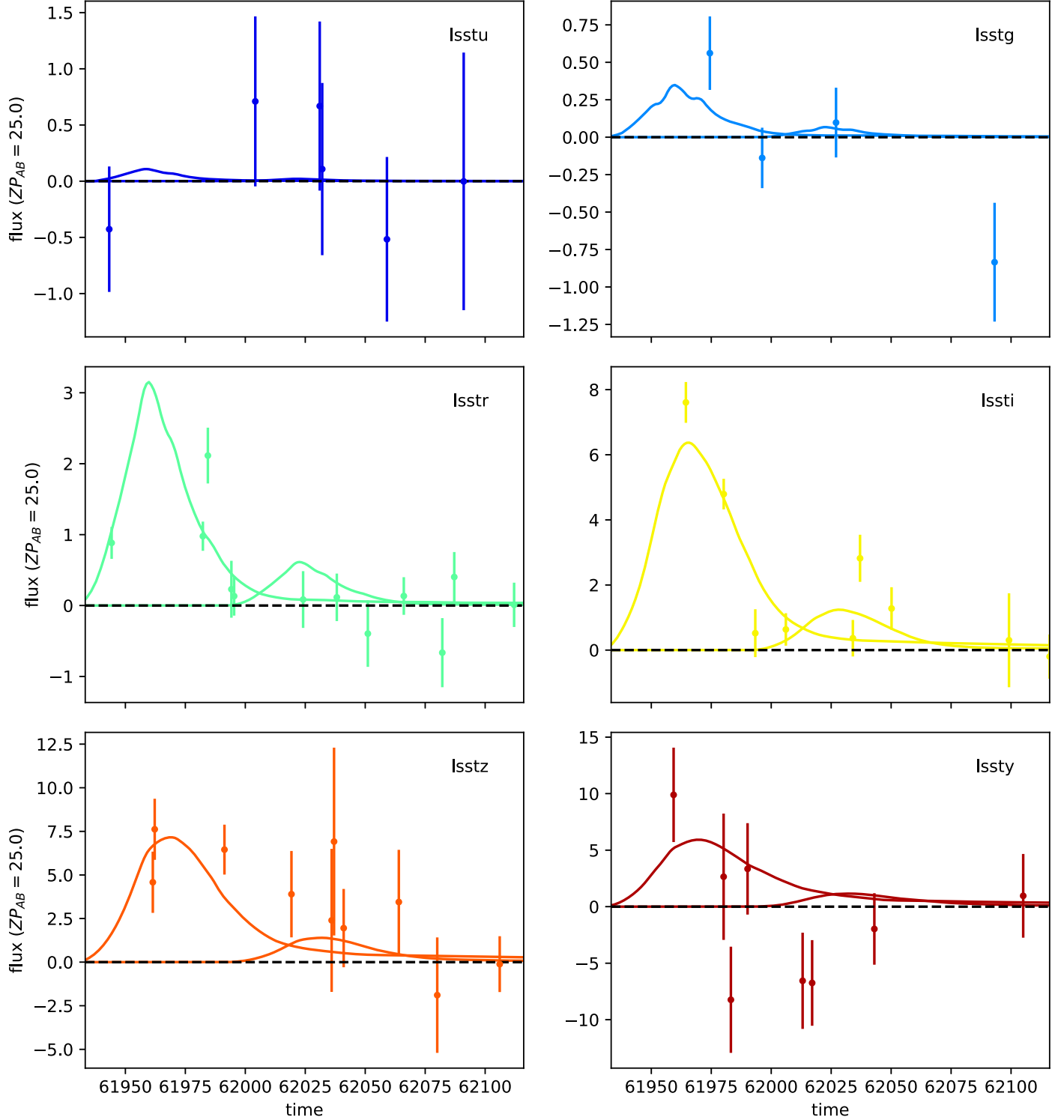


**Figure 28.** Simulated LSST minion\_1016 light curves of a gLSN Ia with two images. The system has  $z_s = 0.98$ ,  $z_l = 0.36$ . The images have a time delay of 62.9 days and lensing amplifications of 3.3 and 0.6. The lines show the model light curves of the individual images. The photometric data are realized from the sum of the model light curves. Single-filter revisits taken within 30 minutes of one another to reject asteroids have been combined via stacking into single light curve points for clarity.

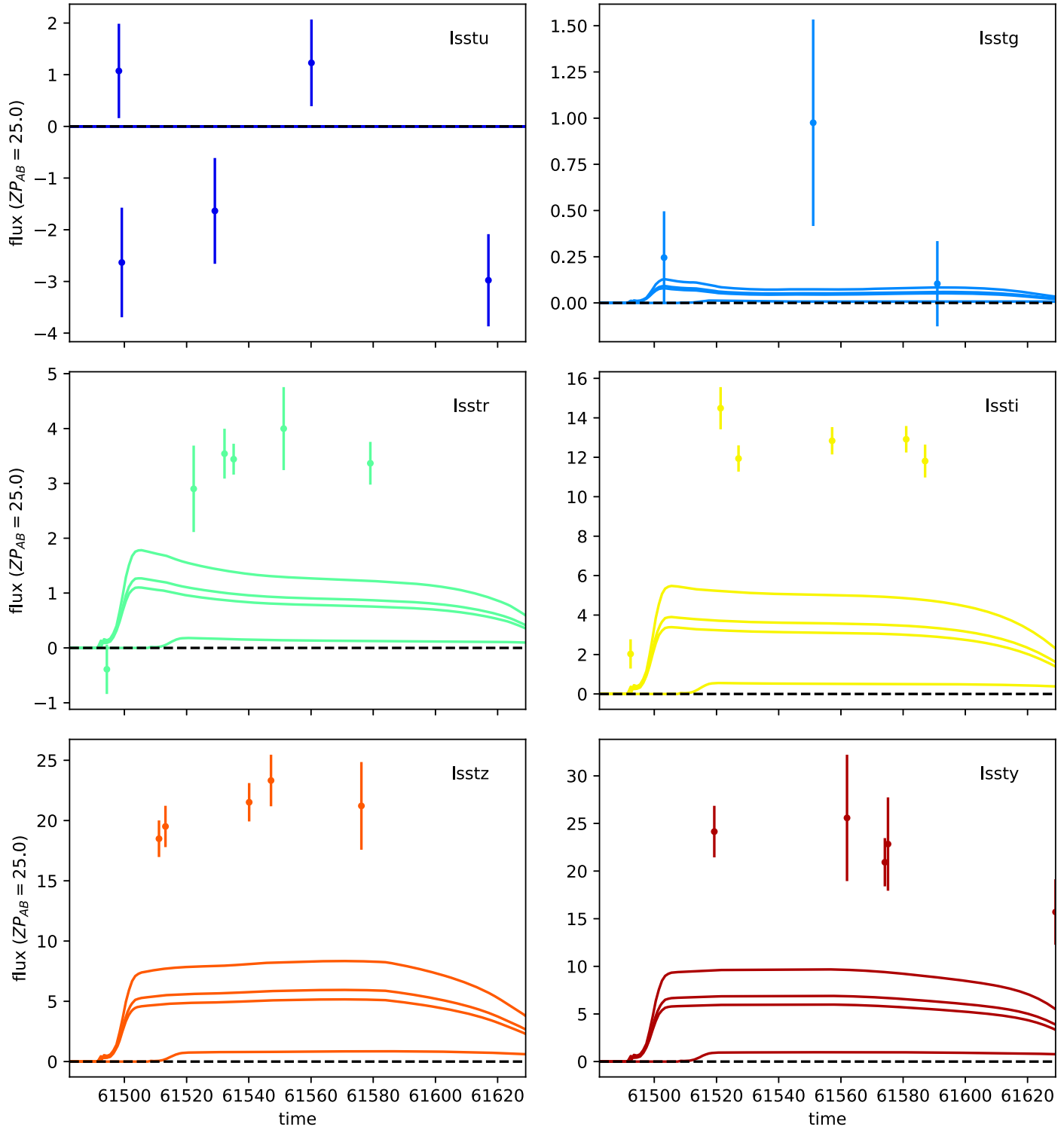


**Figure 29.** Simulated LSST minion\_1016 light curves of a gLSN IIP with four images. The system has  $z_s = 0.58$ ,  $z_l = 0.17$ . The images have time delays relative to the earliest image of 0.16, 15.66, and 0.46 days and lensing amplifications of 8.6, 9.9, 1.4, and 13.8. The lines show the model light curves of the individual images. The photometric data are realized from the sum of the model light curves. Single-filter revisits taken within 30 minutes of one another to reject asteroids have been combined via stacking into single light curve points for clarity.

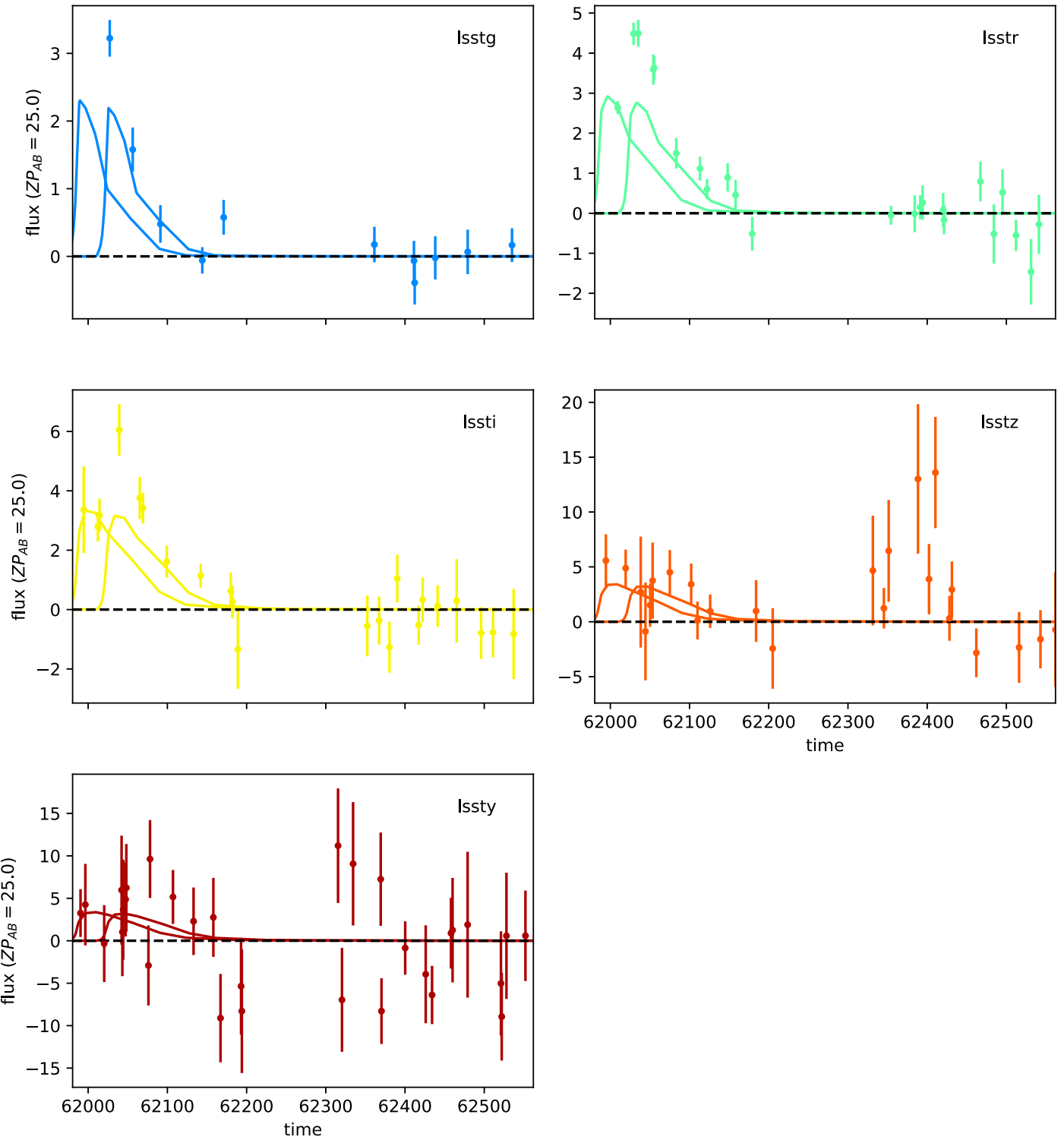


**Figure 30.** Simulated LSST minion\_1016 light curves of a gLSN II with two images. The system has  $z_s = 1.52$ ,  $z_l = 0.21$ . The images have a time delay of 36.8 days and lensing amplifications of 1.8 and 1.7. The lines show the model light curves of the individual images. The photometric data are realized from the sum of the model light curves. Single-filter revisits taken within 30 minutes of one another to reject asteroids have been combined via stacking into single light curve points for clarity.

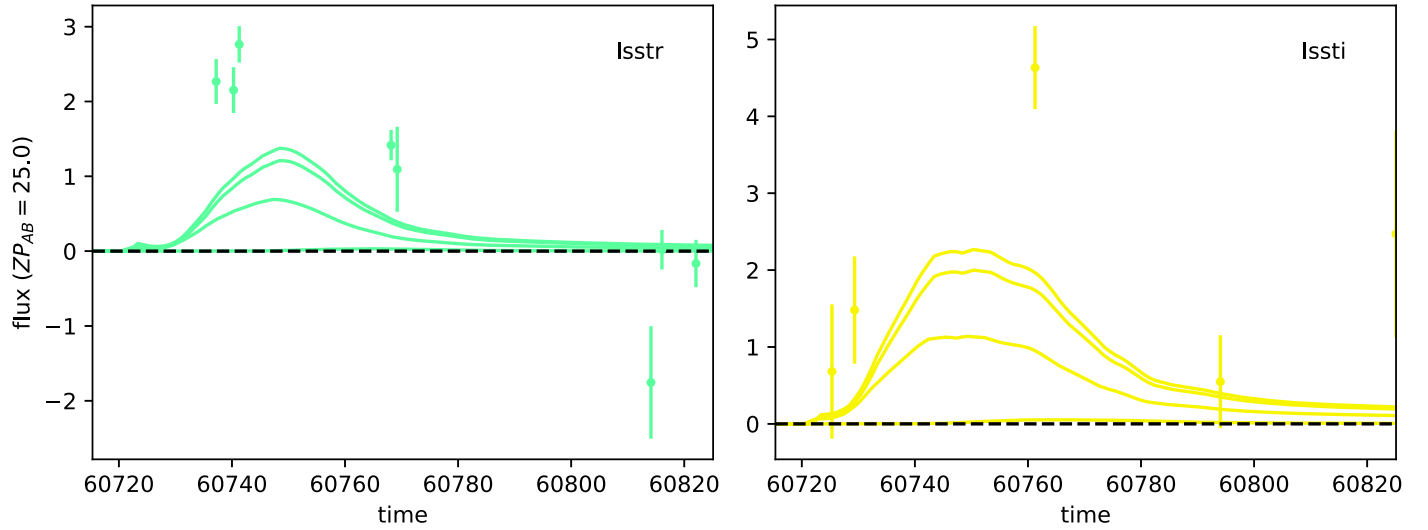


**Figure 31.** Simulated LSST `minion_1016` light curves of a gLSN Ib/c with four images. The system has  $z_s = 0.68$ ,  $z_l = 0.22$ . The images have time delays relative to the earliest image of 1.26, 1.17, and 16.73 days and lensing amplifications of 2.65, 4.64, 5.27, and 0.12. The lines show the model light curves of the individual images. The photometric data are realized from the sum of the model light curves. Single-filter revisits taken within 30 minutes of one another to reject asteroids have been combined via stacking into single light curve points for clarity.

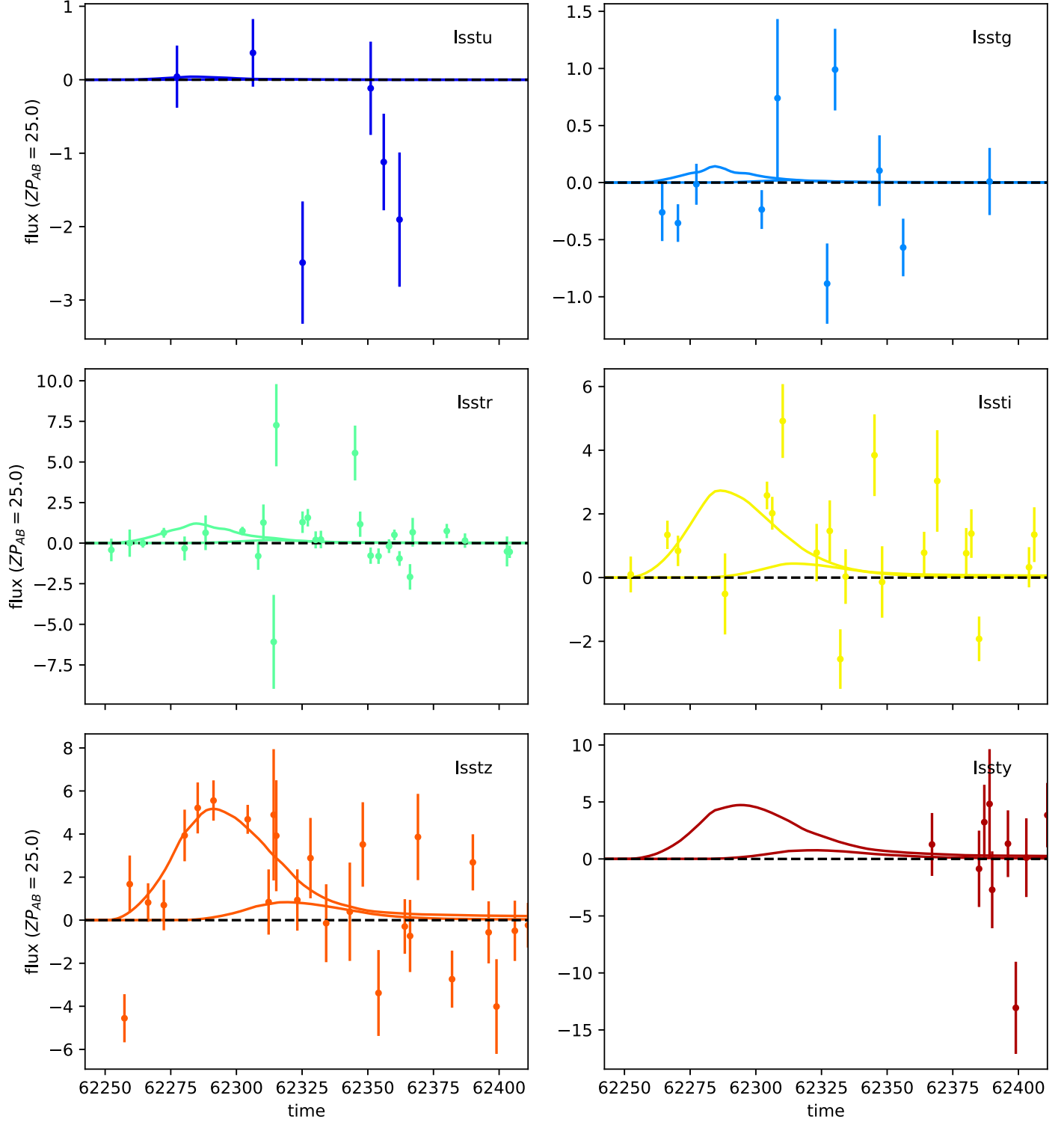


**Figure 32.** Simulated LSST alt-sched light curves of a gLSN Ia with two images. The system has  $z_s = 1.17$ ,  $z_l = 0.19$ . The images have time delays relative to the earliest image of 1.26, 1.17, and 16.73 days and lensing amplifications of 2.65, 4.64, 5.27, and 0.12. The lines show the model light curves of the individual images. The photometric data are realized from the sum of the model light curves.

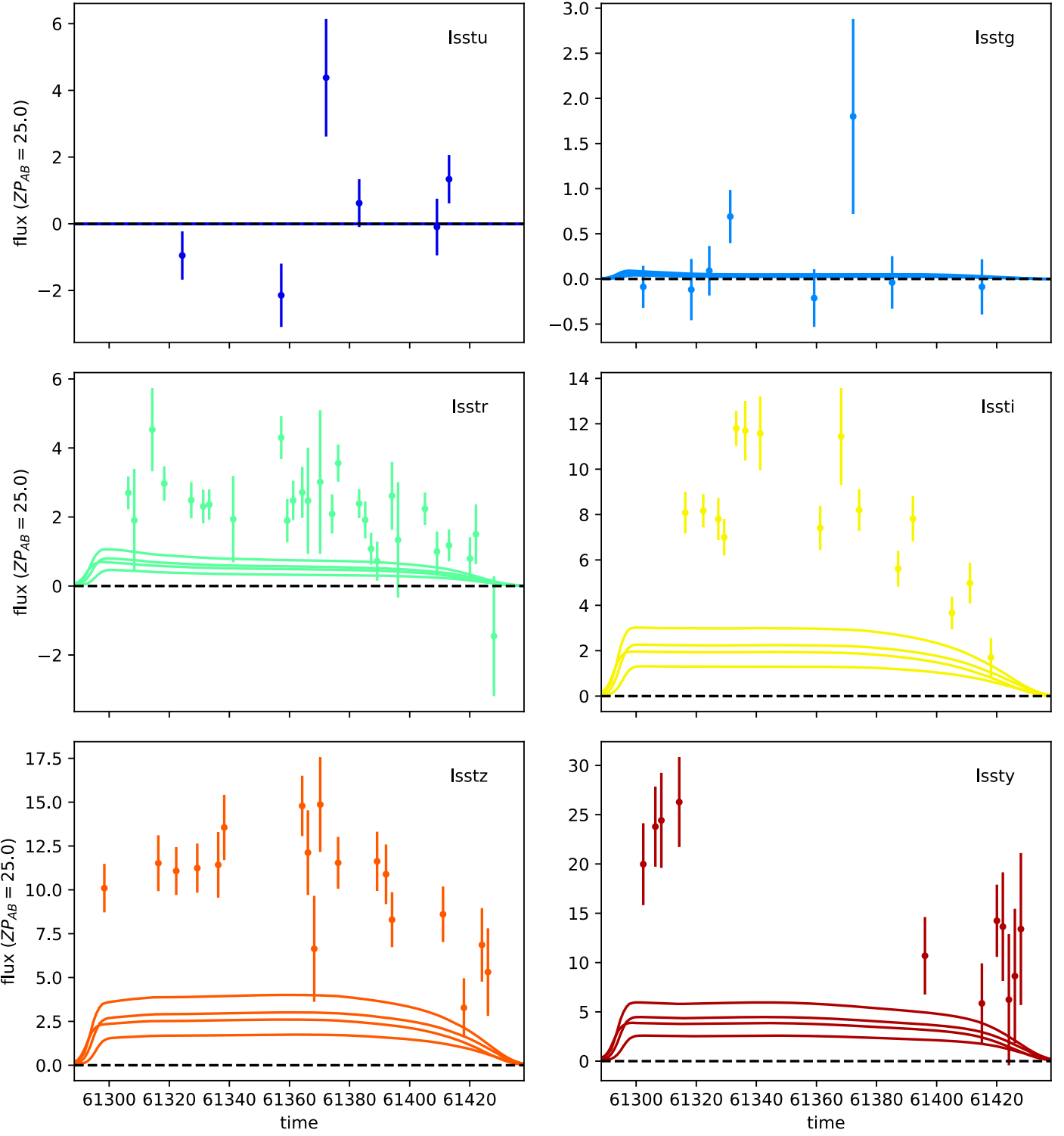


**Figure 33.** Simulated LSST altshed light curves of a gLSN IIP with four images. The system has  $z_s = 0.53$ ,  $z_l = 0.14$ . The images have time delays relative to the earliest image of 1.32, 1.90, and 3.00 days and lensing amplifications of 4.05, 6.23, 4.68, and 2.71. The lines show the model light curves of the individual images. The photometric data are realized from the sum of the model light curves.

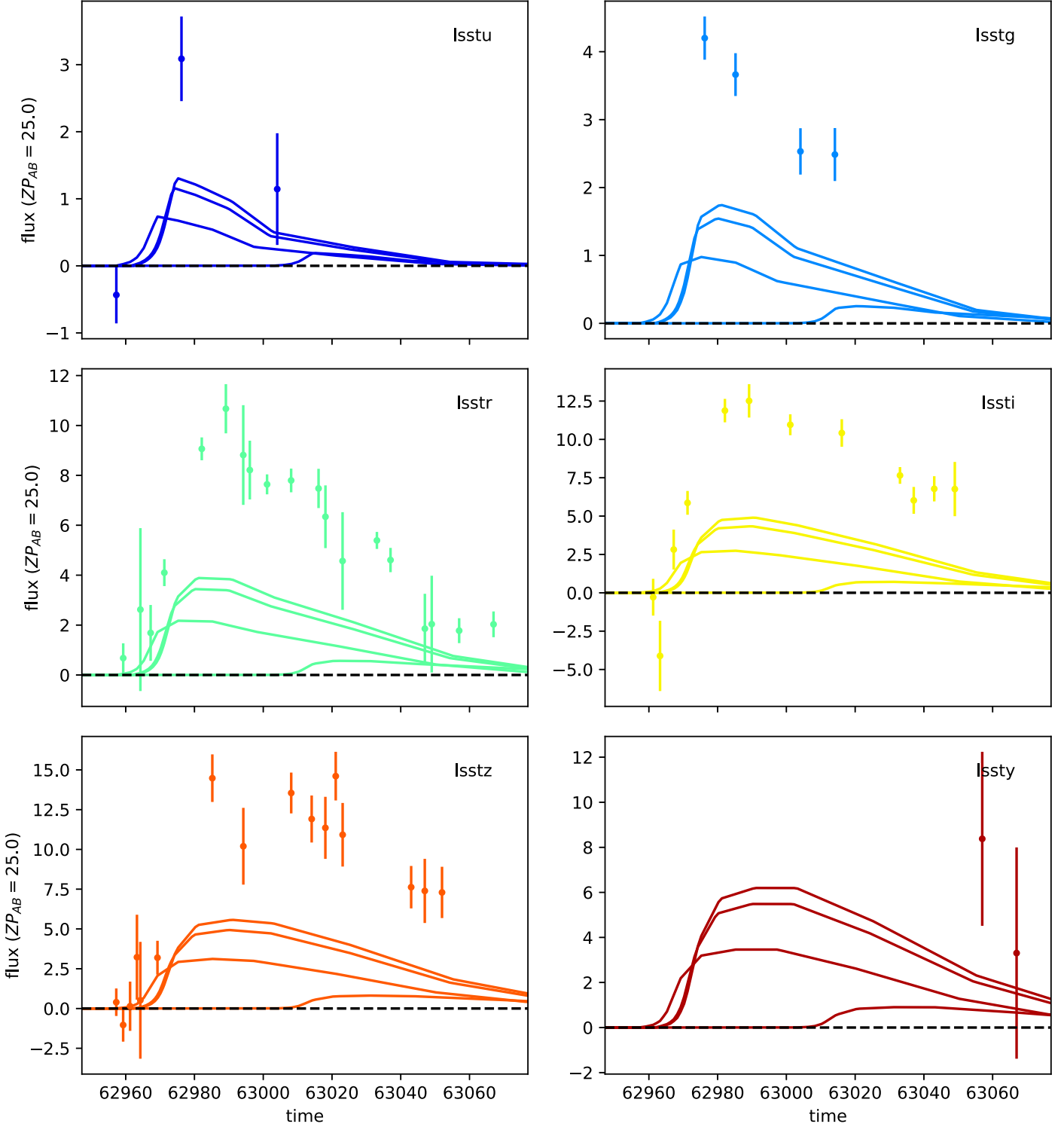


**Figure 34.** Simulated LSST alt-sched light curves of a gLSN II with four images. The system has  $z_s = 1.02$ ,  $z_l = 0.46$ . The images have time delays relative to the earliest image of 45.37, 5.49, and 4.59 days and lensing amplifications of 4.7, 1.2, 8.4, and 7.4. The lines show the model light curves of the individual images. The photometric data are realized from the sum of the model light curves.

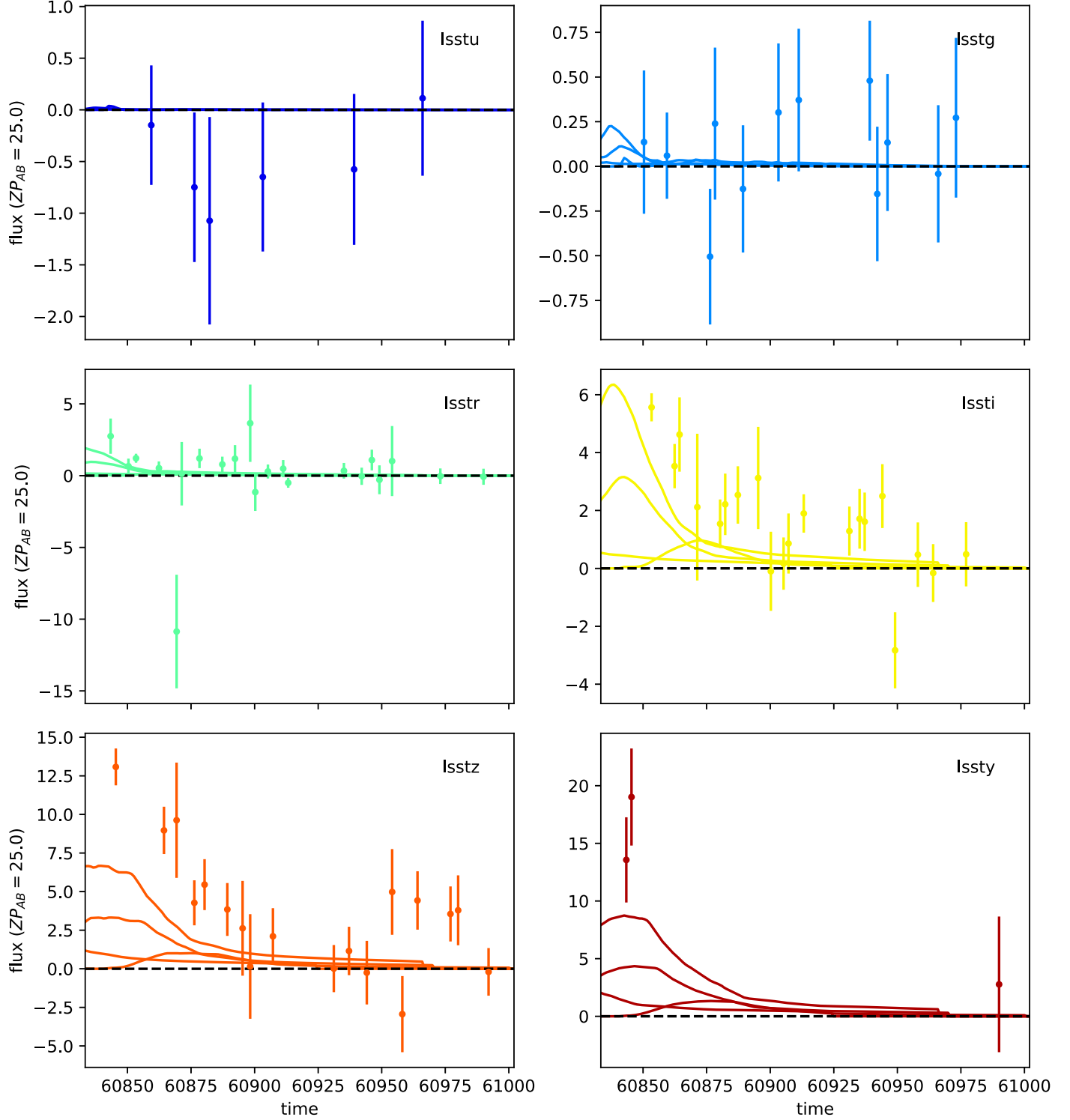
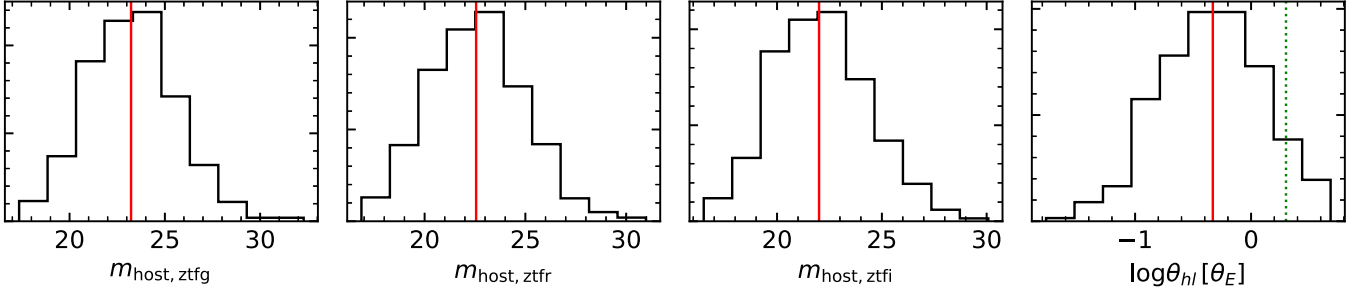
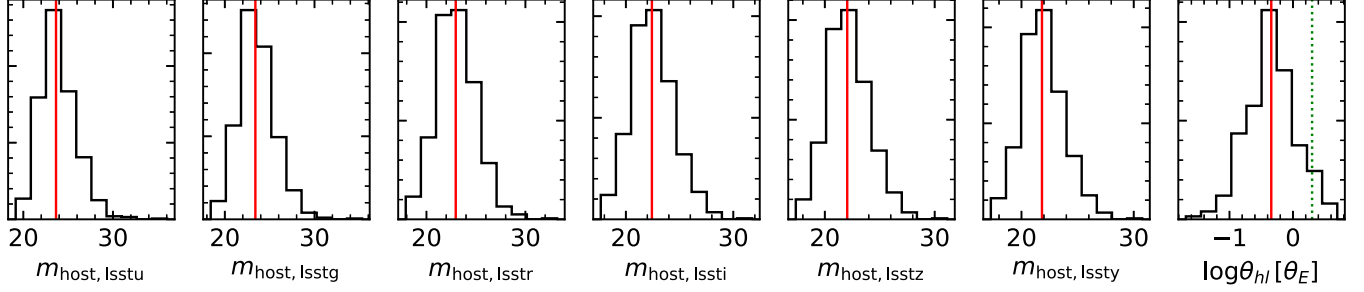


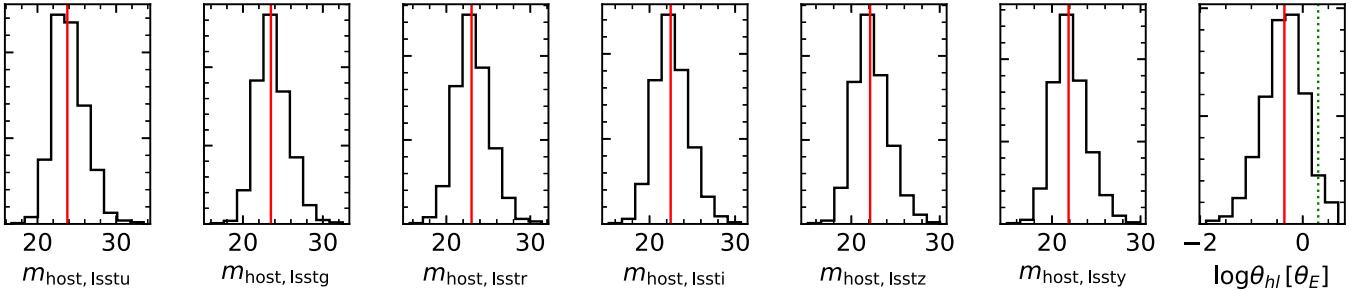
**Figure 35.** Simulated LSST alt-sched light curves of a gLSN Ib/c with four images. The system has  $z_s = 0.88$ ,  $z_l = 0.25$ . The images have time delays relative to the earliest image of 46.44, 42.42, and 76.43 days and lensing amplifications of 1.8, 1.4, 2.8, and 0.4. The lines show the model light curves of the individual images. The photometric data are realized from the sum of the model light curves.



(a) Apparent magnitude [AB] and host-lens separation distributions for ZTF gLSN host galaxies (all SN types).



(b) Apparent magnitude [AB] and host-lens separation distributions for LSST (minion\_1016) gLSN host galaxies (all SN types).



(c) Apparent magnitude [AB] and host-lens separation distributions for LSST (altsched) gLSN host galaxies (all SN types).

**Figure 36.** Lensed host galaxy property distributions for the three surveys considered in this analysis. Red vertical lines indicate medians. The quantity  $\theta_{hl}$  gives the separation between the unlensed position of the host galaxy centroid and the lens galaxy centroid in units of the Einstein radius  $\theta_E$ . Hosts with centroids separated from the lens centroid by less than  $2\theta_E$  (green dashed line) have a significant likelihood of being multiply imaged and can thus provide significant constraints on the lens model after the supernova has faded.

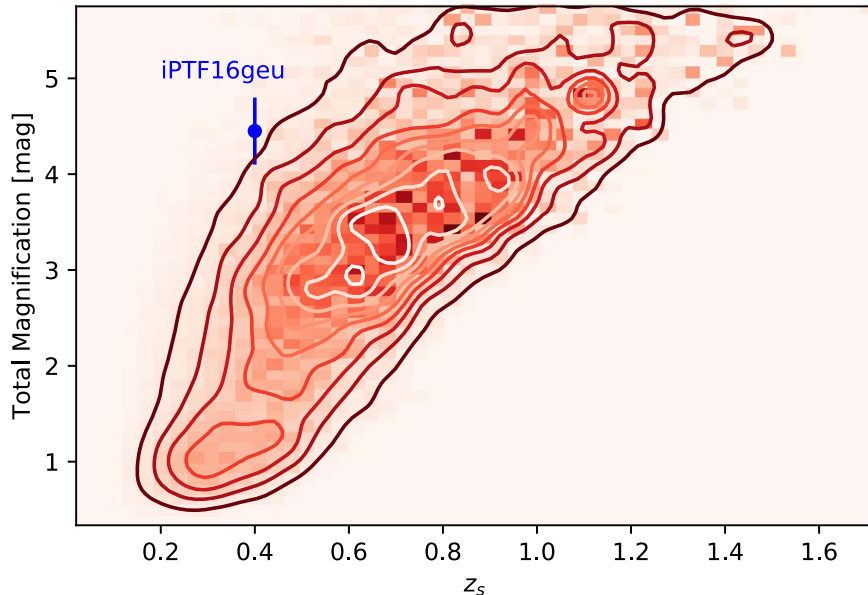


**Figure 37.** Joint distribution of lensing amplification and source redshift for gLSNe Ia found by the simulated ZTF survey and lensed by smooth galaxy lenses. iPTF16geu, marked with a blue star, was dramatically more magnified than expected at its redshift. Additional events are necessary to address the origin of this discrepancy.

D.A.G. gratefully acknowledges Masamune Oguri for sharing the *glafic* source code, which made the Monte Carlo simulations in this paper significantly more efficient, an anonymous referee for comments that significantly improved the clarity of the paper, Ravi Gupta for useful conversations about supernova host galaxies, Tom Collett for improving the deflector mass model, Eric Bellm for sharing his simulated ZTF survey, and Rollin Thomas and Shane Canon for assistance with shifter at NERSC. D.A.G. acknowledges support from Hubble Fellowship grant HST-HF2-51408.001-A. Support for program number HST-HF2-51408.001-A is provided by NASA through a grant from the Space Telescope Science Institute, which is operated by the Association of Universities for Research in Astronomy under NASA contract NAS5-26555. A.G. acknowledges funding from the Swedish Research Council and the Swedish National Space Agency. D.A.G. and P.E.N. acknowledge support from the DOE under grant DE-AC02-05CH11231, Analytical Modeling for Extreme-Scale Computing Environments. This research used resources of the National Energy Research Scientific Computing Center, a DOE Office of Science User Facility supported by the Office of Science of the U.S. Department of Energy under Contract No. DE-AC02-05CH11231.

### ORCID IDs

Daniel A. Goldstein [ID](https://orcid.org/0000-0003-3461-8661) <https://orcid.org/0000-0003-3461-8661>  
 Peter E. Nugent [ID](https://orcid.org/0000-0002-3389-0586) <https://orcid.org/0000-0002-3389-0586>  
 Ariel Goobar [ID](https://orcid.org/0000-0002-4163-4996) <https://orcid.org/0000-0002-4163-4996>

### References

- Amanullah, R., Johansson, J., Goobar, A., et al. 2015, *MNRAS*, 453, 3300  
 Arcavi, I., Gal-Yam, A., Kasliwal, M. M., et al. 2010, *ApJ*, 721, 777  
 Bazin, G., Palanque-Delabrouille, N., Rich, J., et al. 2009, *A&A*, 499, 653  
 Bellm, E. C., Kulkarni, S. R., Barlow, T., et al. 2019, *PASP*, 131, 068003  
 Bellm, E. C., Kulkarni, S. R., Graham, M. J., et al. 2018, *PASP*, 131, 018002  
 Bernardi, M., Sheth, R. K., Annis, J., et al. 2003, *AJ*, 125, 1866  
 Bertin, E., & Arnouts, S. 1996, *A&AS*, 117, 393

- Bezanson, R., van Dokkum, P. G., Franx, M., et al. 2011, *ApJL*, 737, L31  
 Birrer, S., Treu, T., Rusu, C. E., et al. 2019, *MNRAS*, 484, 4726  
 Bonvin, V., Courbin, F., Suyu, S. H., et al. 2017, *MNRAS*, 465, 4914  
 Bridle, S., Shawe-Taylor, J., Amara, A., et al. 2009, *AnApS*, 3, 6  
 Bulla, M., Goobar, A., & Dhawan, S. 2018, *MNRAS*, 479, 3663  
 Cardelli, J. A., Clayton, G. C., & Mathis, J. S. 1989, *ApJ*, 345, 245  
 Chae, K.-H. 2003, *MNRAS*, 346, 746  
 Chae, K.-H. 2007, *ApJL*, 658, L71  
 Choi, Y.-Y., Park, C., & Vogeley, M. S. 2007, *ApJ*, 658, 884  
 Collett, T. E. 2015, *ApJ*, 811, 20  
 Collett, T. E., & Cunningham, S. D. 2016, *MNRAS*, 462, 3255  
 Delgado, F., Saha, A., Chandrasekharan, S., et al. 2014, *Proc. SPIE*, 9150, 915015  
 Djorgovski, S., & Davis, M. 1987, *ApJ*, 313, 59  
 Dobler, G., & Keeton, C. R. 2006, *ApJ*, 653, 1391  
 Einstein, A. 1936, *Sci*, 84, 506  
 Foxley-Marrable, M., Collett, T. E., Verner, G., Goldstein, D. A., & Bacon, D. 2018, *MNRAS*, 478, 508  
 Gilliland, R. L., Nugent, P. E., & Phillips, M. M. 1999, *ApJ*, 521, 30  
 Goldstein, D. A., D’Andrea, C. B., Fischer, J. A., et al. 2015, *AJ*, 150, 82  
 Goldstein, D. A., & Nugent, P. E. 2017, *ApJL*, 834, L5  
 Goldstein, D. A., Nugent, P. E., Kasen, D. N., & Collett, T. E. 2018, *ApJ*, 855, 22  
 Goobar, A., Amanullah, R., Kulkarni, S. R., et al. 2017, *Sci*, 356, 291  
 Graham, A. W., & Driver, S. P. 2005, *PASA*, 22, 118  
 Graham, M. J., Kulkarni, S. R., Bellm, E. C., et al. 2019, *PASP*, 131, 078001  
 Griffith, R. L., Cooper, M. C., Newman, J. A., et al. 2012, *ApJS*, 200, 9  
 Grillo, C., Rosati, P., Suyu, S. H., et al. 2018, *ApJ*, 860, 94  
 Gupta, R. R., Kuhlmann, S., Kovacs, E., et al. 2016, *AJ*, 152, 154  
 Guy, J., Astier, P., Baumont, S., et al. 2007, *A&A*, 466, 11  
 Hakobyan, A. A., Adibekyan, V. Z., Aramyan, L. S., et al. 2012, *A&A*, 544, A81  
 Han, D.-H., Park, C., Choi, Y.-Y., & Park, M.-G. 2010, *ApJ*, 724, 502  
 Hatano, K., Branch, D., & Deaton, J. 1998, *ApJ*, 502, 177  
 Häußler, B., Barden, M., Bamford, S. P., & Rojas, A. 2011, in ASP Conf. Ser. 442, Astronomical Data Analysis Software and Systems XX, ed. I. N. Evans et al. (San Francisco, CA: ASP), 155  
 Häußler, B., McIntosh, D. H., Barden, M., et al. 2007, *ApJS*, 172, 615  
 Holz, D. E. 2001, *ApJL*, 556, L71  
 Hsiao, E. Y., Conley, A., Howell, D. A., et al. 2007, *ApJ*, 663, 1187  
 Keeton, C. R., Kochanek, C. S., & Seljak, U. 1997, *ApJ*, 482, 604  
 Kelly, P. L., Brammer, G., Selsing, J., et al. 2016, *ApJ*, 831, 205  
 Kelly, P. L., & Kirshner, R. P. 2012, *ApJ*, 759, 107  
 Kelly, P. L., Rodney, S. A., Treu, T., et al. 2015, *Sci*, 347, 1123  
 Kinney, A. L., Calzetti, D., Bohlin, R. C., et al. 1996, *ApJ*, 467, 38  
 Kochanek, C. S. 1991, *ApJ*, 373, 354

- Kolatt, T. S., & Bartelmann, M. 1998, *MNRAS*, **296**, 763
- Koopmans, L. V. E., Bolton, A., Treu, T., et al. 2009, *ApJL*, **703**, L51
- Kormann, R., Schneider, P., & Bartelmann, M. 1994, *A&A*, **284**, 285
- Lackner, C. N., & Gunn, J. E. 2012, *MNRAS*, **421**, 2277
- Law, N. M., Kulkarni, S. R., Dekany, R. G., et al. 2009, *PASP*, **121**, 1395
- Levan, A., Nugent, P., Fruchter, A., et al. 2005, *ApJ*, **624**, 880
- Li, W., Leaman, J., Chornock, R., et al. 2011, *MNRAS*, **412**, 1441
- Linder, E. V., Schneider, P., & Wagoner, R. V. 1988, *ApJ*, **324**, 786
- LSST Science Collaboration, Abell, P. A., Allison, J., et al. 2009, arXiv:[0912.0201](#)
- LSST Science Collaboration, Marshall, P., & Anguita, T. 2017, LSST Science Collaborators Observing Strategy White Paper: Science-driven Optimization of the LSST Observing Strategy, Zenodo, doi:[10.5281/zenodo.842713](#)
- Maoz, D., Mannucci, F., & Nelemans, G. 2014, *ARA&A*, **52**, 107
- More, A., Suyu, S. H., Oguri, M., More, S., & Lee, C.-H. 2017, *ApJL*, **835**, L25
- Nugent, P., Kim, A., & Perlmutter, S. 2002, *PASP*, **114**, 803
- Oguri, M. 2010, *PASJ*, **62**, 1017
- Oguri, M., Inada, N., Strauss, M. A., et al. 2008, *AJ*, **135**, 512
- Oguri, M., & Marshall, P. J. 2010, *MNRAS*, **405**, 2579
- Pain, R., Fabbro, S., Sullivan, M., et al. 2002, *ApJ*, **577**, 120
- Peng, C. Y., Ho, L. C., Impey, C. D., & Rix, H.-W. 2002, *AJ*, **124**, 266
- Petrushevska, T., Amanullah, R., Goobar, A., et al. 2016, *A&A*, **594**, A54
- Planck Collaboration, Ade, P. A. R., Aghanim, N., et al. 2016, *A&A*, **594**, A13
- Refsdal, S. 1964a, *MNRAS*, **128**, 295
- Refsdal, S. 1964b, *MNRAS*, **128**, 307
- Richardson, D., Jenkins, R. L. III, Wright, J., & Maddox, L. 2014, *AJ*, **147**, 118
- Riess, A. G., Casertano, S., Yuan, W., Macri, L. M., & Scolnic, D. 2019, *ApJ*, **876**, 85
- Rowe, B. T. P., Jarvis, M., Mandelbaum, R., et al. 2015, *A&C*, **10**, 121
- Sako, M., Bassett, B., Connolly, B., et al. 2011, *ApJ*, **738**, 162
- Schlafly, E. F., & Finkbeiner, D. P. 2011, *ApJ*, **737**, 103
- Schlegel, D. J., Finkbeiner, D. P., & Davis, M. 1998, *ApJ*, **500**, 525
- Schneider, P., & Wagoner, R. V. 1987, *ApJ*, **314**, 154
- Scoville, N., Aussel, H., Brusa, M., et al. 2007, *ApJS*, **172**, 1
- Sérsic, J. L. 1963, BAAA, **6**, 41
- Shen, S., Mo, H. J., White, S. D. M., et al. 2003, *MNRAS*, **343**, 978
- Sheth, R. K., Bernardi, M., Schechter, P. L., et al. 2003, *ApJ*, **594**, 225
- Shu, Y., Bolton, A. S., Mao, S., et al. 2018, *ApJ*, **864**, 91
- Smith, M., Nichol, R. C., Dilday, B., et al. 2012, *ApJ*, **755**, 61
- Smith, R., Dekany, R. G., & Reiley, D. J. 2014, *Proc. SPIE*, **9147**, 914779
- Spergel, D., Gehrels, N., Breckinridge, J., et al. 2013, arXiv:[1305.5422](#)
- Stritzinger, M. D., Taddia, F., Burns, C. R., et al. 2018, *A&A*, **609**, A135
- Sullivan, M., Ellis, R., Nugent, P., Smail, I., & Madau, P. 2000, *MNRAS*, **319**, 549
- Sullivan, M., Le Borgne, D., Pritchett, C. J., et al. 2006, *ApJ*, **648**, 868
- Suwa, Y. 2018, *MNRAS*, **474**, 2612
- Suyu, S. H., Bonvin, V., Courbin, F., et al. 2017, *MNRAS*, **468**, 2590
- Vega-Ferrero, J., Diego, J. M., Miranda, V., & Bernstein, G. M. 2018, *ApJL*, **853**, L31
- Witt, H. J., & Mao, S. 1997, *MNRAS*, **291**, 211
- Wong, K. C., Keeton, C. R., Williams, K. A., Momcheva, I. G., & Zabludoff, A. I. 2011, *ApJ*, **726**, 84
- Yahalom, D. A., Schechter, P. L., & Wambsganss, J. 2017, arXiv:[1711.07919](#)
- Zwicky, F. 1937, *PhRv*, **51**, 290